

Clinopyroxene/melt trace-element-partitioning in sodic alkaline magmas

Charles Beard^{a,*}, Vincent van Hinsberg^a, John Stix^a, Max Wilke^{b,c}

^a*Earth and Planetary Sciences, McGill University, 3450 University Street, Montreal, Québec, H3A 0E8, Canada*

^b*Institut für Erd- und Umweltwissenschaften, Universität Potsdam, Golm, Germany*

^c*Chemie und Physik der Geomaterialien, Deutsches GeoForschungsZentrum GFZ, Potsdam, Germany*

Abstract

Clinopyroxene is a key fractionating phase in alkaline magmatic systems, but its impact on metal-enrichment processes, and the formation of REE + HFSE mineralisation in particular, are not well understood. To constrain the control of clinopyroxene on REE + HFSE behaviour in sodic (per)alkaline magmas, a series of internally heated pressure vessel experiments was performed to determine clinopyroxene-melt element-partitioning systematics. Synthetic tephriphonolite to phonolite compositions were run H_2O -saturated at 650–825°C with oxygen fugacity buffered to $\log fO_2 \approx \Delta QFM + 1$ or $\log fO_2 \approx \Delta QFM + 5$. Clinopyroxene-glass pairs from basanitic to phonolitic fall deposits from Tenerife, Canary Islands, were also measured to complement our experimentally derived data set.

The REE partition coefficients are 0.3–53, typically 2–6, with minima for high-aegirine clinopyroxene. Diopsidic-rich clinopyroxene (Ae_{5-25}) prefer the MREE and have high REE partition coefficients (D_{Eu} up to 53, D_{Sm} up to 47). As clinopyroxene become more Na- and less Ca-rich (Ae_{25-50}), REE incorporation becomes less favourable, and both the M1 and M2 sites expand (to 0.79 Å and 1.12 Å), increasing D_{LREE}/D_{MREE} . Above Ae_{50} , both M sites shrink slightly and HREE ($V^I r_i \leq 0.9 \text{ \AA} \approx Y$) partition strongly onto the M1 site, consistent with a reduced charge penalty for $\text{REE} \leftrightarrow \text{Fe}^{3+}$ substitution.

Our data, complemented with an extensive literature database, constrain a model that predicts trace-element-partition coefficients between clinopyroxene and silicate melt using only mineral major-element compositions, temperature and pressure as input. The model is calibrated for use over a wide compositional range and can be used to interrogate clinopyroxene from a variety of natural systems to determine the trace-element concentrations in their source melts, or to forward model the trace-element evolution of tholeiitic mafic to evolved peralkaline magmatic systems.

Keywords: rare earth elements, aegirine, experimental petrology, Canary Islands, phonolite, peralkaline

1. Introduction

Sodic clinopyroxene appear to more readily incorporate REE than their calcic equivalents (Marks et al., 2004), but despite fractionation of these minerals, melts in evolved alkaline systems can attain high REE contents, even up to economic levels (Kogarko, 1990; Downes et al., 2005; Marks et al., 2011; Sjöqvist et al., 2013; Goodenough et al., 2016; Möller and Williams-Jones, 2016). Trace-element data may be used to model magmatic processes (Spera and Bohrson, 2001; Troll and Schmincke, 2002; Boudreau, 2004; Xu et al., 2010; Girnis et al., 2013; Mungall and Brenan, 2014), but

their interpretation requires precise knowledge of mineral/liquid element-partition coefficients. The approach has been applied to studies of mafic systems and mantle melting processes (Niu, 2004; Workman and Hart, 2005; Foley et al., 2013; Coumans et al., 2016; Peters et al., 2017). However, poor constraints on element-partitioning behaviour in alkaline and peralkaline rocks thus far preclude widespread application in these systems.

Experimental investigations of element-partitioning behaviour in alkali-enriched systems are limited in terms of composition (Wood and Trigila, 2001; Huang et al., 2006), and none yet have explored peralkaline conditions where molar $(\text{Na}+\text{K})/\text{Al}$ exceeds 1. Additional information has been obtained from natural samples by measuring the concentration ratios

*corresponding author

Email address: charles.beard@mail.mcgill.ca (Charles Beard)

of phenocryst–glass pairs from volcanic and intrusive rocks (Larsen, 1979; Wörner et al., 1983; Shearer and Larsen, 1994; Severs et al., 2009; Fedele et al., 2009; Mollo et al., 2016). However, these results may be biased by the presence of melt inclusions, mineral inclusions and mineral zoning, and their interpretation is commonly complicated by unknown or poorly constrained P-T-H₂O-fO₂ conditions of equilibration and assumptions of closed-system behaviour.

In this contribution, we present trace-element-partition coefficients between sodic clinopyroxene and silicate melts of tephriphonolite to phonolite composition, as determined from internally heated pressure vessel experiments on synthetic and natural compositions. These are complemented by well-constrained natural volcanic phenocryst–glass pairs from Canary Islands pyroclastic fall deposits. We characterise the mineral compositional controls on element-partitioning behaviour and present a predictive model for clinopyroxene/melt element-partitioning that can be used to generate clinopyroxene/melt partition coefficients using only clinopyroxene major-element compositions (e.g., as measured by electron-microprobe). This approach permits forward modelling of element budgets during differentiation processes in magmatic systems, including evolved sodic alkaline systems, as well as providing a mineral-based tool that can be used to reconstruct parental melt compositions from clinopyroxene compositions in natural rocks.

2. Methodology

2.1. Experiment starting materials

Clinopyroxene were synthesised in sodic alkaline melts of varying composition to obtain a range of mineral compositions consistent with those in natural systems. Starting glass compositions are given in Table 1 and Figure S1. Synthetic glasses L1 and L5 were prepared from reagent-grade oxide and carbonate powders, ground together in an agate mortar, decarbonated for 6 hrs at 450°C, then homogenised in air for 3 hrs at 1400°C in a Pt crucible. Repeated fusion and grinding in agate ensured chemical homogeneity of the starting glasses, which was confirmed by electron-microprobe analyses of the final fused glass. Finely-ground Mud Tank zircon was added to the homogeneous major-element glasses as a source of Zr, Hf, Nb and Ta; the glasses were then fused for a further three hours at 1400°C. The remaining trace-elements were added as a cocktail of single element nitrate solutions (ICP-MS standards), dried onto the powdered glasses,

then denitrified at 450°C for 30 minutes. The synthetic basanite L1 and phonolite L5 were mixed in varying proportions to make the low alkali (L) series of starting glasses, while dried NaOH and KOH powders were added to make the middle (M) and high (H) alkali starting glasses. Analyses of glass compositions L5 and H5, quenched from superliquidus conditions, confirm that Henry's law was respected (Supplement S1).

A well-mixed rock powder from the Nechalacho Layered Suite in Canada (Möller and Williams-Jones, 2016, Unit NLS-9, sample L09-194-405.5, alternative sample name VM 11-6) was used as experimental starting material for a more extreme peralkaline composition. This composition was not fused prior to loading into experiment capsules, so as to preserve the original volatile-element concentrations. An experiment using this material that was quenched from superliquidus conditions is homogeneous with respect to major-elements, as determined from electron-microprobe measurements.

2.2. Experimental equipment and procedures

In total, 36 partitioning experiments were conducted in a Harwood-type internally heated pressure vessel (IHPV) in the HP-GeoMatS laboratory at the German GeoForschungsZentrum (Table S1). Temperature was measured with Type-S thermocouples calibrated against the melting point of NaCl (Borchert et al., 2010, accuracy of ± 5 °C at 200 MPa). Argon gas was used as the pressure medium, and pressure was measured with a strain gauge to an accuracy of ± 7 MPa. During the experiments, pressure was controlled automatically and held within ± 5 MPa of stated values.

Oxygen fugacity was buffered to the intrinsic redox conditions of the experimental setup, which corresponds to $\log f\text{O}_2 \text{ ca. } \Delta\text{QFM} + 1$ in our H₂O-saturated charges (see Chou, 1986; Berndt et al., 2002; Jugo et al., 2010). One experiment using the Nechalacho Layered Suite composition was performed in a double capsule with a haematite solid buffer, designed to increase $f\text{O}_2$ and promote crystallisation of Fe³⁺-rich clinopyroxene (Eugster and Wones, 1962). This experiment ran at the Hm-Mt buffer, which corresponds to $\log f\text{O}_2 \approx \Delta\text{QFM} + 5$, as confirmed by presence of both buffer minerals in the outer capsule following quench. The experiments were designed to run between the liquidus and solidus for each composition, which corresponds to temperatures between 650 and 825°C, all at 200 MPa pressure (Table S1).

Powdered starting glass and distilled, deionised water were welded inside 3.0 or 3.5 mm outer diameter platinum capsules of 20–25 mm length (see Table S1). To verify that capsules were sealed, they were heated

to 110°C and weighed before and after. The amount of water sealed inside the capsules varied with temperature and composition and was kept in excess of saturation (Carroll and Blank, 1997; Moore et al., 1998; Schmidt and Behrens, 2008). Water saturation was confirmed post-run by puncturing capsules and checking for water expulsion and mass loss on drying at 110°C.

The capsules were loaded into the vessel, pressurised to 200 MPa, then heated to superliquidus temperatures for at least 16 hrs (Table S1) to permit homogenisation of trace-element concentrations, dissolution of water and equilibration of fO_2 by exchange of H₂ through the capsule wall (cf. Gaillard et al., 2002). Following homogenisation, temperature was lowered to run conditions. An initial set of experiments were cooled rapidly from homogenisation to run temperature at about 100°C/min. A second set of experiments were cooled to run temperature at 1°C/min to promote slow growth of crystals and to minimise the formation of compositional gradients in the melt. Vessel temperature was then cycled between run temperature and run temperature + 10°C to promote dissolution of small crystals at the expense of larger grains, and to promote crystal growth close to the run temperature. Element partitioning results are consistent among experiments of different cooling paths. In all experiments, run temperature was kept constant for at least 40 hrs to allow for chemical homogenisation of melt and growth of crystals via Ostwald ripening. Capsules were then quenched to room temperature.

To minimise the growth of groundmass crystals on cooling, a rapid-quench apparatus was used where possible (Table 2). We have not measured quench rates in this vessel, but the capsules probably cooled at rates of several hundred degrees Celcius per second (e.g. Berndt et al., 2002). For the rest of the experiments, quenching was achieved by cutting power to the furnace, which resulted in cooling to below the glass-transition temperature (< 350°C; Giordano et al., 2005) in less than 150 seconds.

2.3. Natural samples

Alkaline volcanism on Tenerife is associated with a weak thermal mantle plume that impinges upon thick, old, slow-moving oceanic lithosphere (Carracedo et al., 2007). This geological scenario has favoured development of a complex magma-plumbing system that produces a great diversity of volcanic products from alkali basalt to phonolite in composition. The Las Cañadas edifice, a large, central, composite stratovolcano (Bryan et al., 1998; Brown et al., 2003; Edgar

et al., 2007), rests upon a base of at least three mafic alkaline shield volcanoes (Thirlwall et al., 2000; Guillou et al., 2004; Gurenko et al., 2006). Xenoliths indicate that a nepheline syenite intrusive system underlies the island (Wiesmaier et al., 2012).

Six clinopyroxene/glass pairs from four different volcanic eruptions on Tenerife have been investigated. The ~ 2 ka eruptive products of Montaña Blanca and Pico Viejo (Ablay et al., 1995) are phonolitic, plinian fall deposits, whereas Montaña Samara is a monogenetic, mafic cinder cone (Albert et al., 2015). Phase-equilibrium experiments conducted on Montaña Blanca unit UMB-II suggest that magma was stored prior to eruption at 850±15°C, 50±20 MPa, with 2.5±0.5 wt% H₂O at log fO_2 ≈ NNO -0.5 (Andújar and Scaillet, 2012). Field locations, mineral proportions and major-element compositions of the clinopyroxene and glasses are presented in Table S1.

2.4. Sample preparation

Experiment capsules were torn open with pliers, and charges were split using a low-speed wafering saw. Samples were mounted in epoxy resin and polished for *in-situ* chemical analyses.

Natural pyroclastic rocks were rinsed in tap water and crushed with a hammer. Crystals and glass fragments, hand-picked from a sieved size-fraction between 1.18 mm and 125 µm, were used to make grain mounts containing 5–20 crystals of clinopyroxene per sample. Natural samples also contain biotite, sanidine, ± spinel, amphibole, olivine, titanite and sodalite. Clinopyroxene mineral mounts were examined using backscattered electron imaging to select euhedral crystals that were free from melt inclusions and chemical zoning (n = 6, Fig. 1).

3. Analytical techniques

All experimental products were examined by reflected-light optical microscopy and scanning electron microscopy, and all phases produced were identified by electron-microprobe using an energy-dispersive detector. Images were obtained to estimate modal proportions of phases, which were calculated using ImageJ freeware (Rasband, 2016, see Table S1).

3.1. Electron-microprobe analysis

Major-element compositions of experimental products and natural minerals and glasses were measured with a JEOL 8900 instrument at McGill University and a JEOL 8230 instrument at the University of Ottawa

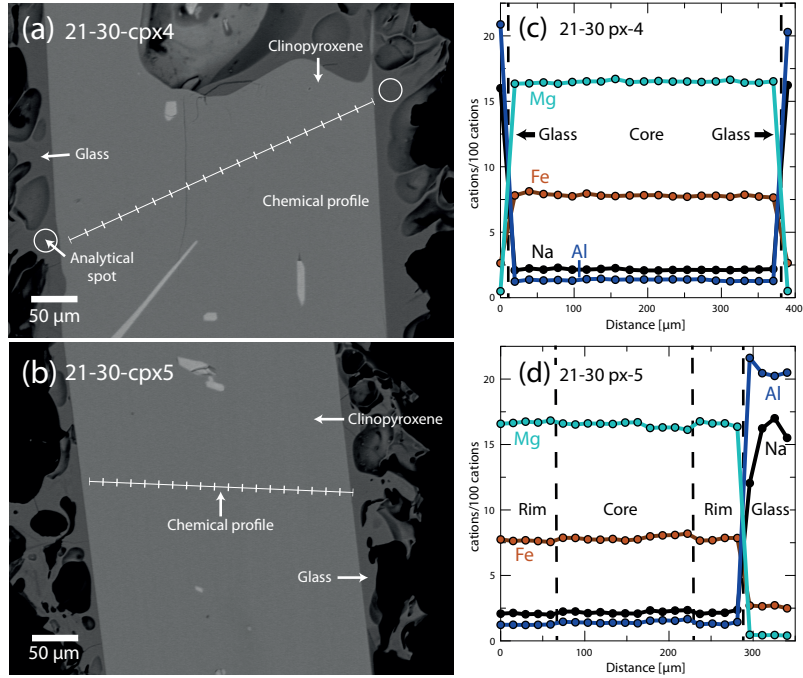


Figure 1: Examples of textural features from Canary Islands clinopyroxene phenocrysts from this study. (a, b) Backscattered electron images show that crystals are euhedral and are free from complex zoning patterns. (c, d) Chemical profiles across clinopyroxene phenocrysts and glass rims (quenched melt), as measured by wavelength dispersive spectroscopy, showing that zoning is effectively absent in these clinopyroxene. In (c) analyses of glass are aligned with the chemical profile shown in (a). Glass analyses shown in (d) are from rims of quenched melt from other clinopyroxene phenocrysts recovered from the same pumice sample. Both pictured phenocrysts are from the basal air fall deposit, associated with the ~2 ka eruption of Pico Viejo, Tenerife (Ablay et al., 1995).

(Table 3). An accelerating voltage of 15 kV was used with a 15 nA beam of 5 μm diameter for minerals, and a 4 nA beam of 50 μm diameter for glasses. Count times for all elements were 60 sec. Using the above routine, we observed no sodium loss over the measurement time period. For the silicate minerals and glasses, both synthetic and natural minerals or oxides were used for calibration (see Table S1). Analytical uncertainties were determined by multiple analyses of reference materials and duplicate analyses of samples.

Element distribution maps were generated with a JEOL 8900 instrument at McGill University using an accelerating voltage of 15 kV, a focussed 40 nA beam, and a dwell time of 50 ms per pixel (Figs. 3, S3). Fe, Ti, Al, Si and Na were measured with wavelength-dispersive detectors, while Ca and Mg were measured with an energy-dispersive spectrometer.

Transects of Ce, Mg and Fe concentrations within the experiment clinopyroxene were measured with a JEOL 8900 instrument at McGill University using a focussed beam of 50 nA with an accelerating voltage of 20 kV. Ce

was counted with a wavelength-dispersive spectrometer with an LIFH crystal for 100 sec (MAC-Ce standard). Mg and Fe were counted for 20 sec, with TAP and LIF crystals respectively (diopside and olivine standards, respectively). Matrix corrections for Mg, Fe and Ce were not possible with these data, for lack of other major-elements measured, however their relative values may still be used to assess the extent to which the clinopyroxene are chemically zoned.

3.2. Laser-ablation ICP-MS

Trace-element concentrations of clinopyroxene and glasses were determined by laser-ablation ICP mass-spectrometry. Analyses were performed at McGill University using a NewWave 213 nm Nd-YAG laser system coupled to a Thermo Finnigan iCAP-Qc quadrupole ICP-MS instrument. Typical fluence was 3–12 J/cm² (from 80 μm to 8 μm spot sizes), with a repetition rate of 10 Hz. Ablated material was transferred to the ICP-MS in a He flow of 800 mL/min and mixed with Ar prior to injection into the plasma. Instrumental drift was

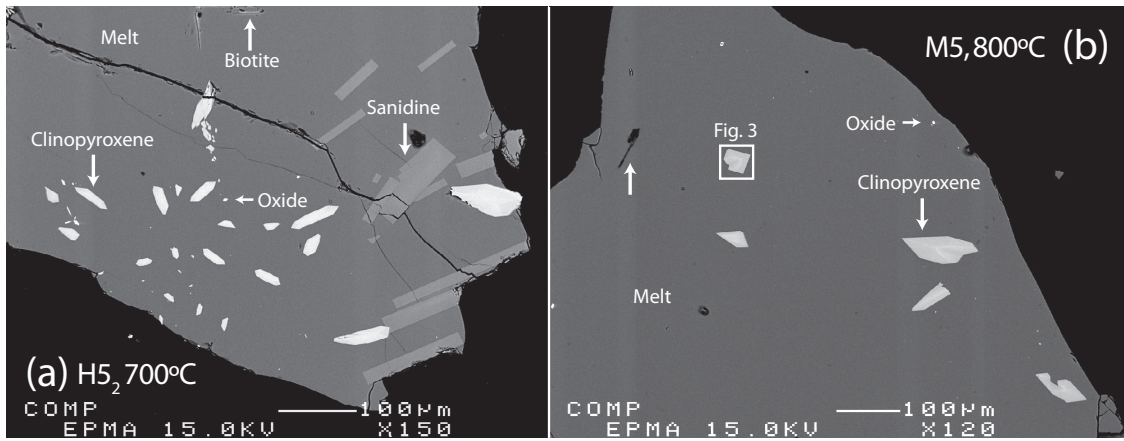


Figure 2: Backscattered electron images showing typical textures of run products from the internally heated pressure vessel experiments. Crystal fractions are typically small (<10% by area), with blade-shaped, euhedral clinopyroxene and glasses free of quench crystals.

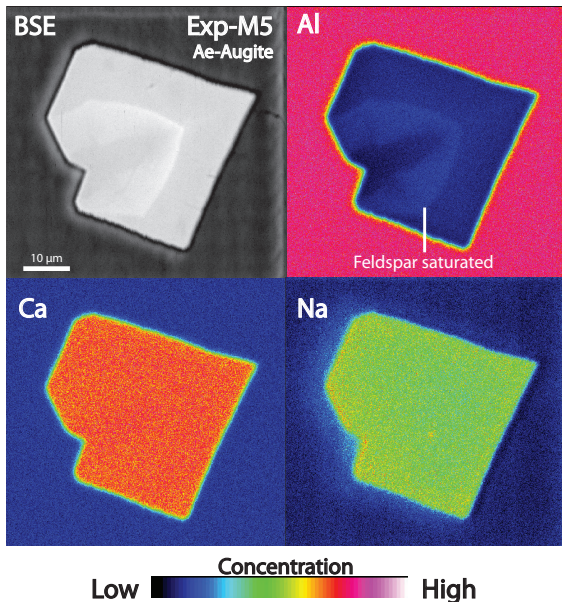


Figure 3: Element maps of clinopyroxene from internally heated pressure vessel experiment M5 (see box in lower magnification image, Fig. 2b). Aegirine-augite clinopyroxene have a sharp internal boundary that reflects feldspar saturation and are subtly zoned. Further element maps are available as an electronic supplement (Fig. S3).

nary Islands clinopyroxene were analysed with beam sizes of 8–80 μm to monitor crater-size-dependent element-fractionation effects; none were found for the elements reported here. For minerals and glasses in the experimental charges, beam sizes of 8–40 μm and 16–80 μm were used, respectively. Depending on grain-size and availability, 5–14 mineral grains and 3–10 areas of glass were analysed per charge. Natural clinopyroxene and rim glasses were analysed using a beam size of 12–80 μm and 12–30 μm , respectively. Wherever possible, ablation was performed along lines parallel to crystal rims (1–3 $\mu\text{m} / \text{sec}$).

Drift corrections and data reduction were conducted in Iolite v2.5 (Paton et al., 2011). The total of major-elements measured by LA-ICP-MS or, where available, the Al concentration from electron-microprobe analyses, was used as an internal standard (Table 3). For some experiments, ablation through the minerals was too rapid to generate a stable signal for data-reduction purposes. In these cases, a mixing model was applied to estimate the composition of these clinopyroxene, similar to those applied by Rubatto and Hermann (2007); Yang et al. (2018)(see supplementary methods S5).

4. Results

4.1. Run product phase stability and crystallinity

Trace-element partition-coefficients are reported for eleven experimental charges. 25 additional experiments were rejected as their run temperatures were superliquidus or subsolidus, or because their growth textures were indicative of disequilibrium (e.g. Fig. S3). Phase proportions are provided in Table S1.

monitored by repeat analyses of the primary standard glass BCR-2G, with bias monitored by repeat analyses of secondary standards UTR-2 peralkaline rhyolite and USGS-RGM-1 rhyolite glasses (Table S1). Sample surfaces were pre-ablated to remove residues from polishing materials and to improve ablation efficiency.

Primary and secondary standards and an unzoned Ca-

All reported experimental runs were near-liquidus (3–22% crystals, RL images) and are characterised by a homogeneous distribution of phases (Fig 2), except for experiments H5₃ and NLS-9_{2-HM}, in which sardine crystals are concentrated at the centre. Glasses are clean, homogeneous and show a limited range of major- and trace-element compositions for each experiment (Fig. S1). Clinopyroxene crystals are generally small, euhedral blades with a narrow range of sizes for a given experiment (<10 µm to 100 µm in cross section, Figs. 2–3). In addition to clinopyroxene and glass, experiments on mafic to intermediate compositions produced magnetite, titanite ± kaersutite amphibole, whereas some phonolitic experiments produced biotite, alkali feldspar ± magnetite (Table S1).

Constraining the full phase equilibria of all of the investigated compositions was beyond the scope of this study. Run conditions and run products given in Supplement S1 provide insight into phase equilibria that might guide future studies. In our experiments it can be seen that clinopyroxene has a wide stability field across the investigated physicochemical conditions, with only a single starting composition generating amphibole in place of pyroxene (experiments L3 and L3₂).

4.2. Glass compositions

All run-product glasses are homogeneous across the length and breadth of the experiment capsules based on multiple electron-microprobe and laser-ablation ICP-MS analyses. Most major-element oxide compositions, as measured by electron-microprobe, show relative standard deviations of < 5% within experiment capsules, with minor-elements oxides (concentration < 1%) showing greater variability, most with standard deviations between 5 and 10 % relative. Trace-element compositions of the glass, as measured by laser-ablation ICP-MS, typically show time-weighted relative standard deviations of 1 to 8% within each capsule, with this variability depending on both the absolute concentration of that element and on the beam-size that was used for analyses (Supplement S1). Low sum-totals of major-element oxide concentrations in the electron-microprobe analyses are a result of high dissolved-water contents in the quenched melt.

On a total-alkalies vs. silica diagram the experiment glasses are predominantly phonolitic in composition, though span the trachyte-phonolite join (Fig. S1). Their alkalinity index (molar (Na + K)/Al) is 0.85 to 1.40, crossing the alkaline–peralkaline join, and the Mg# of these quenched melts is 0 (Mg-free) to 22. The dissolved water content of these quenched melts is 8.8 to 10.7 wt.% (by difference method from EPMA data,

with the Fe oxidation state assigned following Kress and Carmichael 1991) and their NBO/T ratios are 0.98 to 1.42 (Mysen et al., 1982, 1985). The halogen content of the synthetic experiments is nominally zero, whereas glasses from the Nechalacho Layered Suite composition experiments typically contain 0.1 % F and 0.02 % Cl by weight.

The Canary Islands glasses are trachytic to phonolitic (CHECK) and are alkaline to weakly peralkaline in composition (alkalinity index of 0.78 to 1.16) with Mg# of 8 to 39. Dissolved water content and NBO/T ratios are not reported for these glasses because of post-eruptive loss of volatiles. These Canary Islands glasses typically contain 0.2 % F and 0.4 % Cl by weight.

To add: a more comprehensive figure showing glass compositions. This could be in the main text, or as a supplement. Added TAS, MgO vs. CaO and AI vs Mg#

4.3. Compositions of the clinopyroxene and major-element exchange

The Canary Islands clinopyroxene are diopside (Di_{60–90}, Ae_{3–20} CHECK) in composition, with most crystals containing about 0.05 c.f.u. ^{IV}Al (in the T site) and 0.02 c.f.u. ^{VI}Ti (in the M1 site, Tables 3 and S1, Fig. 4). Experiments on the synthetic compositions produced clinopyroxene of diopside to aegirine-augite composition, a subset of which overlap with the compositional space defined by the Canary Islands clinopyroxene on a diopside–hedenbergite–aegirine ternary diagram (Fig. 4a). This low-aegirine group of synthetic clinopyroxene display a positive correlation between ^{IV}Al and ^{VI}Ti content (red, *low aegirine*, Ae_{5–25}), and notably contain both of these elements at elevated concentration relative to the Canary Islands clinopyroxene (^{IV}Al = 0.20–0.45 c.f.u., ^{VI}Ti = 0.07–0.17 c.f.u.). A further subset of synthetic clinopyroxene have higher aegirine content (blue, *med aegirine*, Ae_{25–50}) and show a similar range of Ti content to the low aegirine synthetic minerals (0.05–0.18 c.f.u.), but a limited range of lower ^{IV}Al content (0.1–0.2 c.f.u., Fig. 4b). Experiments performed on the Nechalacho Layered Suite composition (NLS-9, NLS-9_{2-HM}, green, *high aegirine*, Ae_{55–95}) reproduced the aegirine-augite to aegirine clinopyroxene from the natural system (Möller and Williams-Jones, 2016) that contain low concentrations of ^{IV}Al (up to 0.14 c.f.u.) and almost no Ti or Mg.

The Canary Islands clinopyroxene that were selected for determination of mineral–melt partition coefficients are free from melt inclusions, suggesting relatively slow rates of crystal growth (Kennedy et al., 1993, Fig. 1). Chemical zonation, if present, is of a similar magnitude

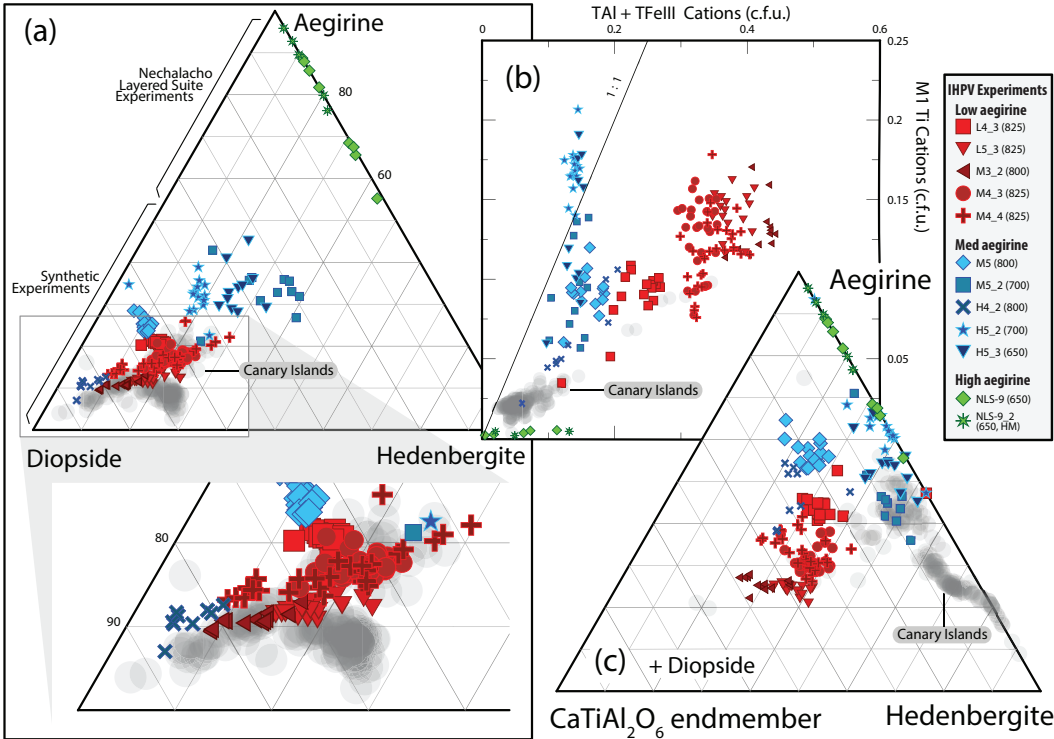


Figure 4: Clinopyroxene grown in internally heated pressure vessel experiments (a) expressed in terms of diopside, hedenbergite and aegirine end-members, (b) their M1Ti and tetrahedral Al and Fe³⁺ contents, and (c) expressed in terms of aegirine, hedenbergite and the theoretical CaTiAl₂O₆ end-member (Akasaka and Onuma, 1980). Clinopyroxene compositions from Canary Islands volcanic rocks are shown for comparison (this study). Fe²⁺/Fe³⁺ within the clinopyroxene was assigned following Droop (1987), then site occupancies and end-member proportions were allocated following Morimoto (1989). For methods used in calculation of the end-member proportions see Supplement S5. The range of clinopyroxene compositions within each experiment records changes to the composition of the melt during crystal growth, whereby the cores of the crystals record the first stage of crystallisation and the rims (highest Fe, Na) are in equilibrium with the quenched melt. **to finish! Also re-plot with a separate symbol to signify Canaries compositions that were used for the derivation of partition coefficients**

407 to the analytical precision of our electron microprobe,
 408 indicating that pressure, temperature and melt composi-
 409 tion remained stable during crystal growth. In the case
 410 of these Canary Islands clinopyroxene, the entire min-
 411 eral is interpreted to be in chemical equilibrium with
 412 the adhered quenched melt. Trace-element abundances
 413 within these Canary Islands clinopyroxene show core-
 414 to-rim variations of about 1–5 % relative, with larger
 415 variations in element abundance associated with sector
 416 zoning than with concentric growth zoning (Supplement
 417 S1). (TO CONFIRM with images)

418 By contrast our experiment clinopyroxene display
 419 systematic compositional variation between their cores
 420 and rims; this variation recording changes to melt com-
 421 position during growth of these crystals (e.g. Fig.
 422 3). The systematics of crystal-chemical zonation
 423 both within individual experimental charges and within
 424 groups of experiments reveal major-element exchange

425 vectors between the clinopyroxene and the melt. Three
 426 major-element exchange mechanisms correspond to the
 427 low (Ae_{5–25}), medium (Ae_{25–50}) and high (Ae_{55–95}) ae-
 428 girine domains defined above (Figs. 4b, 5 and S4).

429 **And may be used to infer.... the composition of the
 430 mineral assemblage that is crystallising? To discuss.
 431 Comments, please!**

432 With increasing alkali content, the Si content in
 433 clinopyroxene increases at the expense of tetrahedrally
 434 co-ordinated Al and Fe³⁺. As aegirine content increases,
 435 substitutions at the tetrahedral site become relatively
 436 less important than exchanges at the M1 and M2 sites.
 437 At the M1 site, the substitution of Ti for ions of 2+ and
 438 3+ valence correlates well with the exchange of tetra-
 439 hedrally coordinated 3+ cations for Si⁴⁺. The exchange
 440 behaviour of 2+ and 3+ cations at the M1 site depends
 441 on the aegirine content of the clinopyroxene. In low-
 442 aegirine clinopyroxene, the concentration of 3+ ions at

443 the M1 site is negatively correlated with X_{Na}^{M2} , whereas
444 in medium- and high-aegirine clinopyroxene, the M1
445 site takes progressively more 3+ ions as X_{Na}^{M2} increases.
446 Substitutions of Ca^{M2} for Na^{M2} are relatively unimpor-
447 tant in low-aegirine clinopyroxene, but play a large role
448 in medium- and high-aegirine exchange vectors.
449

450 Suites of Canary Islands clinopyroxene follow simi-
451 lar major-element exchange systematics to our low ae-
452 girine experiment clinopyroxenes (CHECK, expand if
453 necessary).

453 4.4. Trace-element concentrations in the experiment 454 clinopyroxene

455 Assessing the homogeneity of trace-element-
456 concentrations within minerals is important when
457 defining equilibrium partition-coefficients because
458 only the rims record true chemical equilibrium with
459 the adjacent melt. Measurements of trace-element-
460 concentrations in experimentally-grown minerals are
461 often challenging as a result of their small size; They
462 are commonly comparable in scale to the beam-size of
463 laser-ablation or SIMS systems ($\sim 10\text{--}20 \mu\text{m}$). In many
464 cases it is therefore not possible to assess the extent to
465 which trace-element-concentrations are zoned within
466 experimentally-grown crystals. To assess the extent to
467 which trace-element-concentrations are zoned within
468 our experiment clinopyroxene, electron-microprobe
469 transects were measured across seven crystals for the
470 elements Mg, Fe and Ce (Supplement S3). Transects
471 were made across grains from three experiments, each
472 crystallised to varying degrees.

473 The electron-microprobe transects reveal that
474 clinopyroxene Ce-concentration follows both sector-
475 zoning and concentric growth-zoning patterns, as
476 recorded by backscattered electron images and the
477 XMg of the clinopyroxene. Sector-zoning has a more
478 pronounced effect on the Ce-concentration in the
479 clinopyroxene than concentric growth-zoning, causing
480 one transect to appear ‘laterally-zoned’ and another to
481 appear ‘reverse-zoned’ in terms of Ce-concentration.
482 These effects are due to sector-zoning, with bright
483 sector-zones on BSE images associated with higher Ce-
484 concentrations than dark zones. To gain insight into the
485 variation in clinopyroxene Ce-concentration associated
486 with concentric growth-zoning, analyses were grouped
487 *per-experiment* to average this sector-zoning effect.
488 Ratios of median average Ce-counts / rim Ce-counts
489 represent the difference between the composition of
490 the bulk crystal, as analysed by LA-ICP-MS, and the
491 composition of the clinopyroxene rims that approach
492 chemical equilibrium with the adjacent quenched melt
493 and have a mean value of 1.08, ranging between 1.04

494 and 1.12. The highest values are found for the largest
495 clinopyroxene crystals and in these, because of their
496 size, we were able to avoid the cores in the analyses
497 via LA-ICP-MS, reducing the growth-zonation bias in
498 trace-element partition-coefficients.

499 Where large clinopyroxene crystals were present
500 and time-averages of element counts could be used
501 for the reduction of laser-ablation data, trace-element-
502 compositions are similar among clinopyroxene crystals
503 within individual experiments (Fig. TO ADD? Table
504 S1) indicating that trace-element concentrations in the
505 melt phase remained spatially homogeneous throughout
506 the duration of the experiments. Typical trace-element
507 concentrations in the experiment clinopyroxene are il-
508 lustrated in Supplementary Figure S5c.

509 5. Discussion

510 5.1. Attainment of equilibrium in the Canary Islands 511 rocks

512 The Canary Islands trace-element partition-
513 coefficients presented here were determined from
514 euhedral, blade-shaped crystals free of melt inclusions
515 and chemical zonation. The corresponding quenched
516 melt was in direct contact with these crystals and shows
517 no zonation in backscattered electron images (Fig. 1).
518 While equilibrium conditions are challenging to con-
519 firm for a natural volcanic system, the euhedral forms,
520 chemical homogeneity of crystals, and congruency
521 between samples from separate eruptions suggest that
522 the crystals grew in a stable environment, and were not
523 subject to chemical or physical perturbations during
524 growth (Fig. 6).

525 5.2. Attainment of equilibrium in the experiments

526 Experiments used to determine trace-element
527 partition-coefficients must have attained, or at least
528 closely approached, chemical equilibrium. Unfortu-
529 nately no experiments are able to determine equilibrium
530 trace-element partition-coefficients *sensu stricto* be-
531 cause reversal experiments, where a clinopyroxene
532 re-equilibrates with a melt, are not possible owing
533 to sluggish diffusion of most elements through the
534 clinopyroxene structure (Van Orman et al., 2001; Zhang
535 et al., 2010). The following two sections discuss some
536 analytical and experimental biases that must be con-
537 sidered when determining mineral-melt trace-element
538 partition-coefficients from crystallisation experiments.

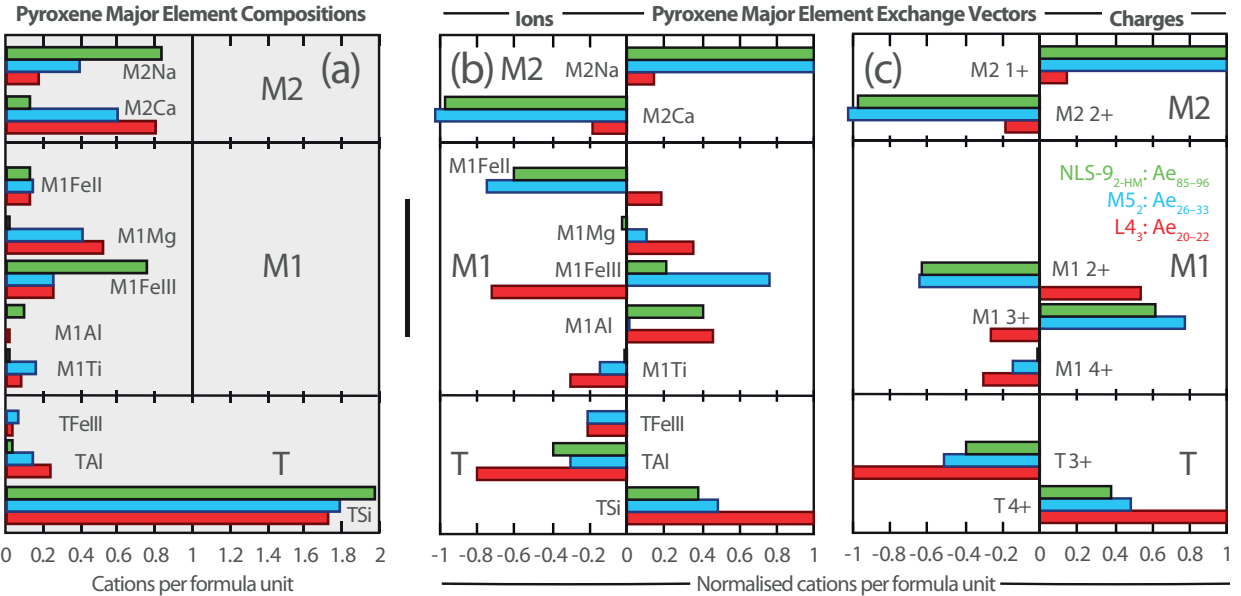


Figure 5: Bar charts showing clinopyroxene composition and major-element exchange mechanisms for three experiments representative of high (green), medium (blue) and low-aegirine (red) clinopyroxene. (a) clinopyroxene major-element compositions are expressed as cations per six-oxygen formula unit (b) exchange mechanisms grouped by ions, (c) grouped by charges. Methods used to calculate these exchange mechanisms are available in the caption of Supplementary Figure S4.

539 5.2.1. The formation of diffusive boundary layers

540 A potential barrier to chemical equilibration during
 541 crystallisation is the formation of a diffusive boundary
 542 layer within the melt adjacent to growing crystals. In
 543 a perfect equilibrium case there are no compositional
 544 gradients in the melt at any time during crystal growth.
 545 However in reality the growth of crystals depletes com-
 546 patible elements from the melt and residually enriches
 547 incompatible elements. Theoretically, this process of
 548 crystal growth results in formation of a (potentially
 549 ephemeral) diffusive boundary layer in the melt directly
 550 adjacent to the crystal that is depleted with respect to
 551 compatible elements and enriched with respect to those
 552 that are incompatible (Lu et al., 1995). The composition
 553 of such a diffusive boundary layer depends on both the
 554 relative enrichment or depletion of elements during the
 555 crystallisation process, and the rate at which these el-
 556 ements diffuse through the melt. Rapidly-diffusing ele-
 557 ments with partition-coefficients close to unity will have
 558 concentrations closest to that of the bulk melt.

559 Experiments designed to investigate trace-element-
 560 partitioning behaviour might employ slow cooling rates
 561 to limit the development of diffusive boundary layers,
 562 thus forming crystals from melt that is closer in com-
 563 position to that of the bulk experiment. Such exper-
 564 iments then run into another problem, in that signif-

565 icant crystallisation may occur at temperatures above
 566 that of the final run temperature. Rapidly-cooled ex-
 567 periments circumnavigate this issue, but may form rel-
 568 atively more pronounced diffusive boundary layers dur-
 569 ing crystal growth that become ‘flattened out’ during the
 570 homogenisation stage of the experiment.

571 Numerous diffusion data have been gathered for sil-
 572 icate melts over the past few decades, and a compre-
 573 hensive review is given by Zhang et al. (2010). Diffu-
 574 sion of trace-elements through water-saturated peralka-
 575 line melts is rapid, owing to their depolymerised struc-
 576 ture. For example Lanthanum diffusion-coefficients are
 577 6 orders of magnitude higher than for water-saturated
 578 granitic compositions of a similar temperature (com-
 579 pare Rapp and Watson, 1986; Behrens and Hahn, 2009).
 580 This rapid diffusion serves to minimise the formation
 581 of diffusive boundary layers adjacent to growing crys-
 582 tals in our experiments. Coupled diffusion mechanisms
 583 complicate the application of measured single-element
 584 diffusion-coefficients to a crystallising system (Grove
 585 et al., 1984; Liang et al., 1994; Costa et al., 2003).
 586 Here, the diffusive flux of trace-elements may be cou-
 587 pled to gradients in major-element concentration within
 588 the melt.

589 To investigate the impact of diffusive effects on trace-
 590 element-partitioning between clinopyroxene and melt,

591 Mollo et al. (2013) performed crystallisation experiments on trachybasaltic melts at a range of cooling rates 642
592 (2.5–50°C / hr). Rapid cooling rates result in depletions 643
593 of Si, Ca and Mg in the clinopyroxene that are compensated 644
594 for by enrichments in Al, Na and Ti. Regardless of 645
595 cooling rate, Ounma parabolae could be fitted through 646
596 isovalent sets of partition-coefficients, indicating that 647
597 crystal-lattice-effects dominated over those associated 648
598 with the formation of diffusive boundary layers and 649
599 that local equilibrium was achieved at the time of crys- 650
600 tallisation. In their rapidly-cooled experiments Mollo 651
601 et al. (2013) found apparent clinopyroxene/melt trace- 652
602 element partition-coefficients that varied with identical 653
603 crystal-chemical systematics to true equilibrium parti- 654
604 tion coefficients, the magnitude of both sets of trace- 655
605 element partition-coefficients following the ^{14}Al con- 656
606 tent of the clinopyroxene (ibid., their Fig. 9). Devi- 657
607 ations of the partition coefficient of several orders of 658
608 magnitude can be obtained only when rapidly growing 659
609 crystals entrap small portions of the diffusive boundary 660
610 layer that are found as minute melt inclusions randomly 661
611 distributed in the mineral phase (Kennedy et al., 1993). 662
612 In this extreme case, partitioning behaviour is obviously 663
613 influenced by contamination phenomena and no Onuma 664
614 parabolae can be derived. As Onuma parabolae could 665
615 successfully be fitted through partitioning data for all of 666
616 our presented experiments (see following sections), and 667
617 no melt inclusions were observed in optical and electron 668
618 imaging, we infer that our data were not affected by the 669
619 presence of such melt inclusions, and that they may be 670
620 compared directly with partitioning data derived from 671
621 experiments that employed slower cooling rates. 672
622

623 5.2.2. Chemical zonation in the experiment clinopyroxene: Theoretical framework 675

624 Trace-elements diffuse slowly through the clinopyroxene 676
625 structure relative to that of the melt (Van Orman et al., 677
626 2001; Zhang et al., 2010), therefore no re-equilibration 678
627 of trace-elements takes place on an experimental time scale. 679
628 Strictly speaking, clinopyroxene only record true equilibrium 680
629 conditions at their outermost rim. Experiments designed for the derivation 681
630 of equilibrium partition coefficients ideally minimise 682
631 bias by limiting the fraction of crystallisation, producing 683
632 minerals that are as homogeneous as possible. Currently available *in situ* analytical 684
633 techniques for trace-element abundances, such as LA-ICP-MS and SIMS, 685
634 are limited in terms of minimum beam-size to $\sim 10\ \mu\text{m}$; 686
635 chemical zonation, however subtle, will be continuous 687
636 from the core to the rim of the mineral. Consequently, 688
637 no experimentally-derived partition-coefficients record 689
638 chemical equilibrium *sensu stricto*, but properly con- 690
639 ducted experiments may closely approximate this state. 691
640

641 Because only the very rim of a crystal records chemical 642 equilibrium with the adjacent melt, and some internal 643 portions of the minerals must be sampled during *in-situ* 644 analyses all experimentally-determined trace-element 645 partition-coefficients are biased toward higher values 646 for compatible elements and lower values for incompatible 647 elements. The magnitude of these biases depends on the 648 fraction of crystallisation in the experiment, the true 649 equilibrium partition-coefficient of that element, as well as 650 the proportion of each growth-zone sampled during the 651 *in-situ* analysis. Fortunately *in-situ* chemical analyses 652 preferentially sample the mantle and rim of zoned crystals 653 because few analyses section a crystal perfectly through the 654 core. As a result there is a sampling bias toward equilibrium 655 mineral compositions.

656 Consider a hypothetical experimental system in which 657 20% of the melt crystallises as a single mineral, and where 658 the chemical analyses of that mineral are truly bulk averages 659 of that mineral composition. An incompatible element with 660 a true equilibrium partition coefficient of 0.1 would return 661 a measured partition coefficient of 0.09, a small bias because 662 the concentration of that incompatible element in the melt 663 changed only subtly during the course of crystallisation. For 664 compatible elements with true D_i values of ~ 10 , measured 665 partition coefficients can be a factor of 2–3 higher than true 666 partition coefficients, because their concentration in the 667 melt changes more than an incompatible element during 668 the course of crystallisation.

669 Further complexity is introduced in systems that crystallise 670 multiple minerals simultaneously. In the case of experiment 671 M3₂, the REE are compatible in clinopyroxene, but are 672 incompatible in biotite and oxides (e.g. Mahood and Stimac, 673 1990; Schmidt et al., 1999). The REE have therefore been 674 residually enriched in the melt phase by the crystallisation 675 of biotite and oxide minerals, while simultaneously being 676 depleted from the melt by crystallisation of clinopyroxene. 677 These two competing processes serve to minimise the effect of 678 fractional crystallisation on the concentration of trace-elements 679 in the melt and consequently derived REE partition- 680 coefficients between clinopyroxene and melt will be 681 closer to true equilibrium values.

682 5.2.3. Implications of the cerium zonation across the 687 experiment clinopyroxene

683 Because of beam-size limitations and the small minerals 684 generated in the majority of our experiments it 685 was not possible to measure all trace-element 686 concentrations within the core and rim of experiment clinopy- 687
688

693 roxene separately. Electron-microprobe analyses offer a
694 smaller minimum beam-size than LA-ICP-MS systems
695 at the expense of precision and of number of elements
696 that may be analysed simultaneously. This higher spa-
697 tial resolution permitted investigation of the zonation of
698 Ce concentrations within the experiment clinopyroxene,
699 with Ce as a proxy for the other compatible elements.

700 The magnitude of concentric growth zoning in the
701 experiment clinopyroxene was examined by averag-
702 ing bulk and rim compositions across multiple sector-
703 zoned grains within each experiment. The median Ce
704 counts divided by the rim Ce counts was 1.04 for ex-
705 periment M3₂, 1.08 for experiment M5 and 1.12 for
706 the fluorine-bearing experiment M3-1.25F (see Beard,
707 2018). Contrary to theory discussed above, the subtly
708 (3%) crystallised experiment M5 shows a greater vari-
709 ation in core-to-rim Ce content than the more heavily
710 (?? TO ADD%) crystallised experiment M3₂. Fur-
711 thermore, the $D_{Ce}^{cpx/melt}$ for experiment M3₂ (6.2) is ap-
712 proximately double that for experiment M5 (see dis-
713 cussion below), which should further promote the for-
714 mation of Cerium zonation in the clinopyroxene during
715 crystallisation. Consequently it is possible that many
716 existing experimentally-derived trace-element partition-
717 coefficients are systematically offset from true equilib-
718 rium values.

719 If Cerium is used as a proxy for the behaviour of com-
720 patible elements in our experimental system, then ap-
721 parent partition coefficients derived for these elements
722 via LA-ICP-MS are systematically offset to higher val-
723 ues by 4–8%. Such a systematic bias is small, relative
724 to the variation in clinopyroxene-melt partition coeffi-
725 cients within our sample set, as well as in the litera-
726 ture. The effect of crystal zonation on incompatible el-
727 ement concentrations was not measured, but as outlined
728 in the theoretical framework above, this effect should be
729 smaller than that for the compatible elements. No cor-
730 rection factor has been applied to the data presented in
731 the figures below, or in Tables 4 and S1.

732 5.3. Trace-element-partitioning

733 Trace-element partition-coefficients and their uncer-
734 tainties were calculated as mass concentration ratios be-
735 tween clinopyroxene and coexisting glass and are re-
736 ported in Tables 4 and S1.

737 Where trace-element-concentrations in clinopyrox-
738 ene could be determined using regular time-averages
739 of counts from the ICP-MS system, a time-weighted
740 average composition of clinopyroxene was used with
741 that of the coexisting glass to calculate trace-element
742 partition-coefficients and their associated uncertainty.

743 Where the laser-ablation unmixing model was required
744 for reduction of clinopyroxene trace-element analyses,
745 the partition coefficients were calculated using time-
746 weighted average compositions of glass alongside the
747 corresponding ‘unmixed’ clinopyroxene trace-element
748 concentration. Because a robust-regression data reduc-
749 tion scheme was used, this technique returns a median-
750 average trace-element concentration for clinopyroxene,
751 whilst effectively rejecting outlier data, for example
752 from the ablation of minerals other than clinopyroxene
753 that may have been hidden below the polished surfaces
754 of the grain mounts. Uncertainty calculations are de-
755 scribed in the caption for Figure S5.

756 Three markedly different behaviours of rare earth
757 element partitioning are observed in the experiments
758 (Fig. 6). These depend on the aegirine concentration
759 in the clinopyroxene and match the major-element ex-
760 change vector domains discussed above. Low-aegirine
761 experiment clinopyroxene (Ae_{5–25}) prefer the MREE;
762 medium-aegirine clinopyroxene (Ae_{25–50}) show a sim-
763 ilar behaviour, save for higher LREE partition coeffi-
764 cients, whereas high-aegirine clinopyroxene (Ae_{55–95})
765 strongly prefer HREE and show incompatible behaviour
766 for the light and middle REE. The experiment REE par-
767 tition coefficients are 0.3–53, typically 2–6, with min-
768 ima for LREE and MREE in high-aegirine clinopyrox-
769 ene (Fig. 6). Our experimental partition coefficients are
770 about an order of magnitude higher than in most other
771 studies of clinopyroxene-melt element-partitioning that
772 were performed on different bulk compositions (Fig.
773 7d,e,f), with the exception of high Si systems, such as
774 the Bandelier Tuff (cf. Olin and Wolff, 2010).

775 The Canary Islands clinopyroxene show similar
776 rare-earth-element partitioning-systematics to the low-
777 aegirine experiment clinopyroxene, with absolute val-
778 ues for these partition coefficients of about one order of
779 magnitude lower.

780 The high field-strength elements (HFSE) Zr, Hf, Nb
781 and Ta are compatible to slightly incompatible in the
782 experimental clinopyroxene, and typically 1–2 orders
783 of magnitude less compatible in the Canary Islands
784 clinopyroxene (Fig. 7a,b,c). The HFSE are most com-
785 patible in sodic clinopyroxene. Partition coefficients for
786 the large-ion lithophile elements K, Sr, Pb are positively
787 correlated with X_{Na}^{M2} in the low- and medium-aegirine
788 clinopyroxene, but are lower in high-aegirine clinopy-
789 roxene (Fig. S6). The Rb, Cs and Ba partition coeffi-
790 cients have a high uncertainty and are maximum esti-
791 mates owing to low concentrations of these elements in
792 the clinopyroxene, close to the detection limit for anal-
793 yses by LA-ICP-MS. These data are therefore not dis-
794 cussed further. Lithium is incompatible ($D_{Li} = 0.1–0.4$)

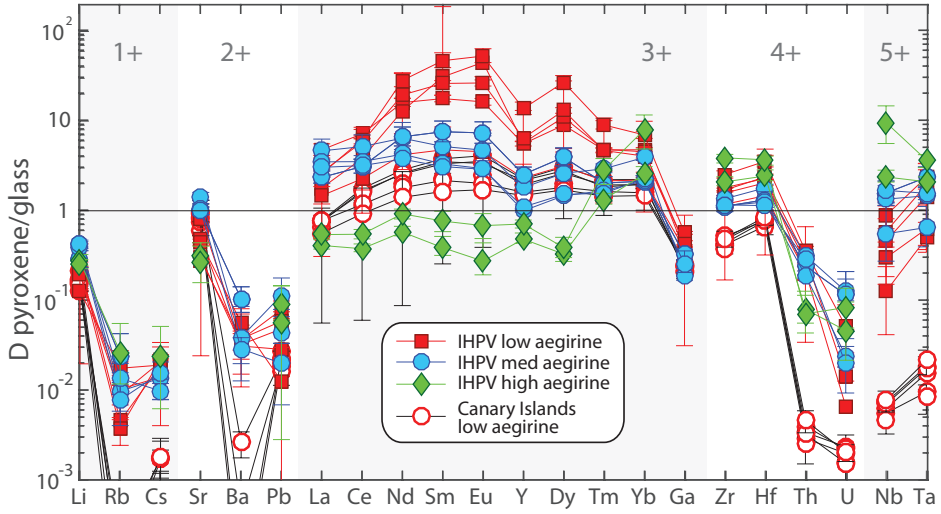


Figure 6: Trace-element partition-coefficients between clinopyroxene and silicate melt, as determined from internally heated pressure vessel experiments ($n = 11$; low-, medium- and high-aegirine types) and from clinopyroxene-rim glass pairs from pyroclastic fall deposits from Tenerife, Canary Islands ($n = 6$; low-aegirine type). Uncertainties on the partition coefficients are at the 1σ level.

in both Canary Islands and experimental clinopyroxene and, like Sr and Pb, becomes more compatible with increasing aegirine content in the clinopyroxene, plateauing at $X_{Na}^{M2} = 0.4$ and decreasing thereafter (Figs. 7g, S6g). The actinides U and Th show contrasting partitioning behaviour; the former showing no correlation with aegirine content in the clinopyroxene, the latter becoming more incompatible with increasing aegirine content (Fig. 7h). The U and Th partition coefficients for our Canary Islands samples are similar to those for the Roman Province (Wood and Trigila, 2001; Fedele et al., 2009; Mollo et al., 2013, 2016), and are 1–2 orders of magnitude more incompatible relative to the experimental clinopyroxene.

5.4. Fits to the lattice-strain model

The equilibrium partitioning of trace-elements between minerals and melts is largely controlled by the structure of the crystal lattice, its elasticity (Onuma et al., 1968; Kumazawa, 1969; Weidner and Vaughan, 1982) and its ability to accommodate an excess or shortage in charge (Blundy et al., 1998; Wood and Blundy, 2001; Hanchar et al., 2001; Corgne and Wood, 2005). The lattice-strain model provides a framework in which the influence of these variables on partitioning behaviour can be quantified, and thus predicted under conditions bracketed by a calibrating data set (Onuma et al., 1968; Blundy and Wood, 1994; Wood and Blundy, 2014). Lattice structure has a dependence on

pressure, temperature and composition, and element-partitioning is a thermodynamically-controlled process (e.g. Wood and Blundy, 1997).

Most trivalent ions, including the REE and Y enter the M2 site of clinopyroxene, which is typically 6- or 8-coordinated (Deer et al., 1992). Smaller trivalent ions, including Al, Cr, Ga, Sc, and in the case of Fe-rich clinopyroxene the HREE may enter the smaller, octahedral M1 site (Olin and Wolff, 2010; Bédard, 2014). The high field-strength elements Ti, Zr, Hf, Nb and Ta are typically hosted by the M1 site (Hill et al., 2000, 2011; Dugert et al., 2014).

To investigate systematics in D_i values and the mechanisms by which trace-elements are incorporated into clinopyroxene, element-partitioning behaviour was explored in light of the lattice-strain theory, quantitatively described by the lattice-strain equation:

$$D_i^{\text{mineral/melt}} = D_0 \exp \left[\frac{-4\pi E_s N_a}{RT} \left(\frac{r_0}{2} (r_0 - r_i)^2 - \frac{1}{3} (r_0 - r_i)^3 \right) \right] \quad (1)$$

where r_0 is the ideal radius for the lattice site, E_s is the Young's modulus (i.e., the lattice site stiffness), D_0 is the strain-free partition coefficient, N_a is Avagadro's number, R is the gas constant, T is temperature in Kelvin, and r_i is the ionic radius of the element in question, all radii in Å. We focused on 3+ ions that cover a wide range of radii and fitted lattice-strain parameters for both the M1 and M2 sites of clinopyroxene (Fig. 8):

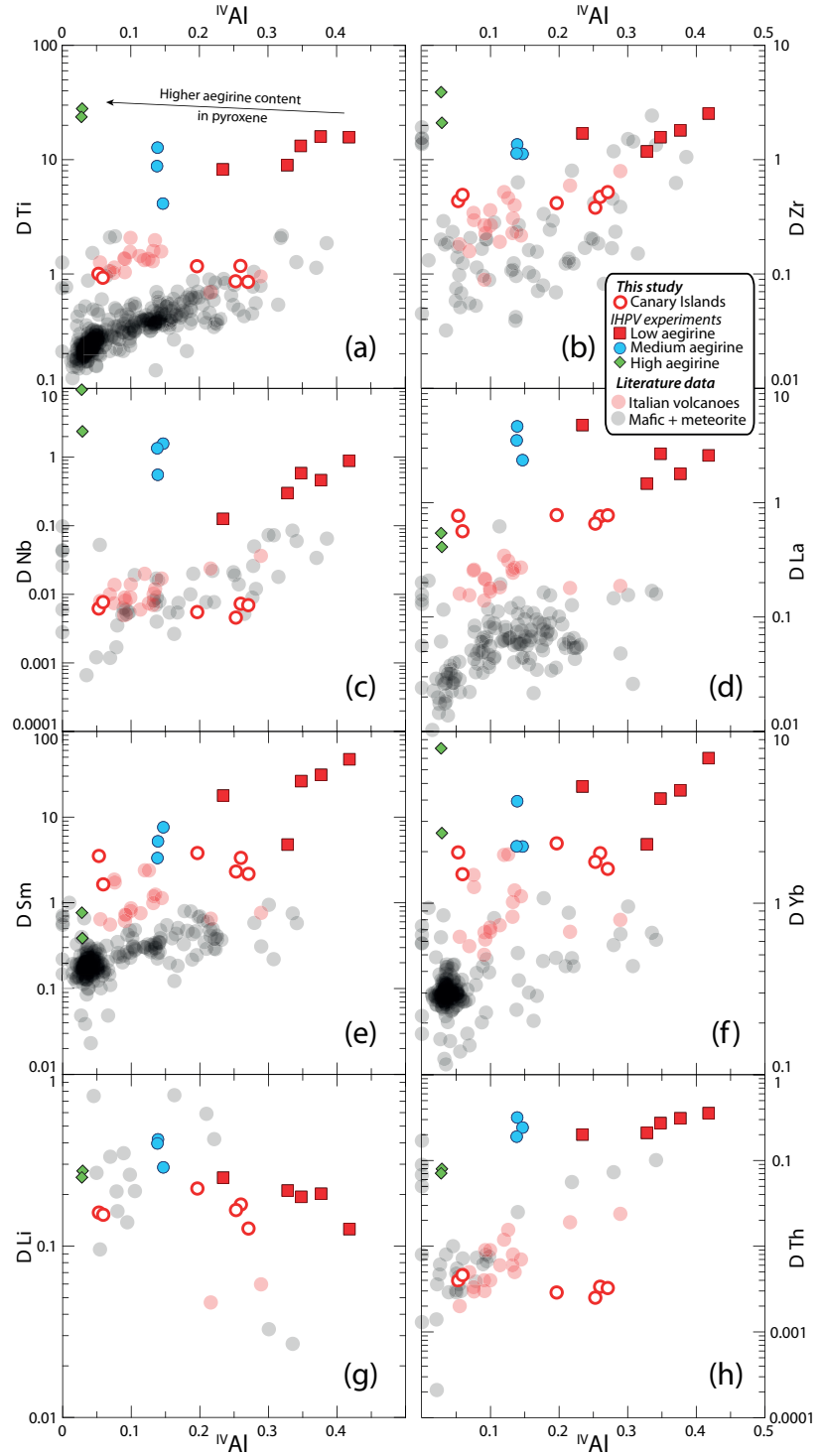


Figure 7: Element partition coefficients for HFSE (Ti, Zr, Nb), REE (La, Sm, Yb) and TE (Li, Th) vs. ^{IV}Al . Literature values ($n = 411$), including those from the Roman Province, Italy, are from the compilation of Bédard (2014), with additional, more recent, data from Mollo et al. (2016). A similar diagram with X_{Na}^{M2} in place of ^{IV}Al is in Supplement S6.

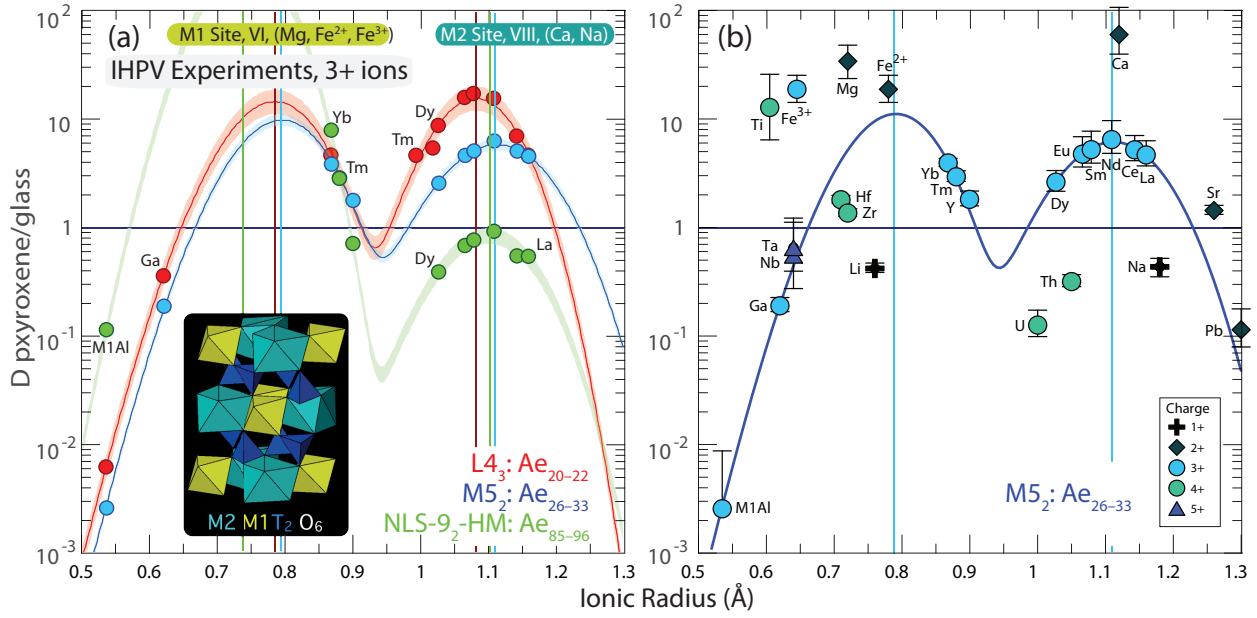


Figure 8: Non-linear weighted least-squares fits to element-partitioning data from the internally heated pressure vessel experiments following the lattice-strain model of Blundy and Wood (1994). (a) Representative fits to 3+ ion partitioning behaviour with examples for low (red), medium (blue) and high-aegirine (green) clinopyroxene experiments. (b) Measured partition coefficients for ions of 1+, 2+, 4+ and 5+ charges that are consistent with the lattice-strain model. Ionic radii are assigned to 6 or 8 fold co-ordination (Shannon, 1976), and were chosen to minimise residuals in the fit (cf. Olin and Wolff, 2010). Y was not included in the fitting routine for 3+ ions because of mass fractionation effects (*ibid.*). Vertical coloured lines indicate ideal ionic radii (r_0) of M1 and M2 sites and shaded areas indicate 95% confidence intervals on the fits determined via bootstrapping. Uncertainties on the partition coefficients in (b) are 1σ . Fitted lattice-strain parameters are given in Table 4.

$$D_i^{cpx/melt} = D_0^{M2} \exp \left[\frac{-4\pi E_s^{M2} N_a}{RT} \left(\frac{r_0^{M2}}{2} (r_0^{M2} - r_i)^2 - \frac{1}{3} (r_0^{M2})^3 \right) \right] + D_0^{M1} \exp \left[\frac{-4\pi E_s^{M1} N_a}{RT} \left(\frac{r_0^{M1}}{2} (r_0^{M1} - r_i)^2 - \frac{1}{3} (r_0^{M1})^3 \right) \right] \quad (2)$$

Parabolae for 3+ ions were fitted for the M1 and M2 sites using the REE, Ga and Al assigned to the M1 site of clinopyroxene (Fig. 8a). Fits are weighted based on uncertainties for the element-partition coefficients. HREE have higher element-partition coefficients than can predicted by substitution into the M2 site, hence were fitted with ionic radii for sixfold coordination into the M1 site (cf. Olin and Wolff, 2010; Reguir et al., 2012). Lattice-strain parameters as obtained from fits to the data are shown in Table S1.

In some low-aegirine experiments and the Canary Islands rocks, lattice-strain fitting for 3+ ions at the M1 site was not possible, because too few HREE partitioned onto the M1 site of these clinopyroxene. Here, we chose to fit only lattice-strain parameters for the M2 site, or fix D_0^{3+} values for the M1 site to match those for the

M2 site, and fit only the r_0 and E_s parameters for the M1 site. Fitting of element-partitioning data for 1+, 2+ and 4+ ions was less successful owing to sparse coverage of suitable radii and detection-limit issues for some elements. Partition coefficients for 1+, 2+, and 4+ elements follow radius- and charge-dependent trends consistent with lattice-strain theory and reported effects of charge on lattice-strain parameters (Fig. 8b, e.g., Hazen and Finger, 1979; Law et al., 2000; Adam and Green, 2006).

5.4.1. Effects of composition on ideal site size, r_0

As the composition of clinopyroxene shifts from augite toward aegirine, the size of the M1 and M2 sites, or strain-free radii (r_0), should diverge following the sizes of the major-element cations on these sites. Lattice-strain fits for 3+ cations indicate expansion of the M2 site between low and medium-aegirine clinopyroxene, with r_{0M2}^{3+} correlating well with Na replacing Ca (Figs. 8, 9). Expansion of the M2 site stalls at $r_{0M2}^{3+} \approx 1.12 \text{ \AA}$ and $X_{Na}^{M2} \approx 0.4$, changing little in size between medium and high-aegirine clinopyroxene. We suggest that this is a ‘saturation effect’, whereby the smaller

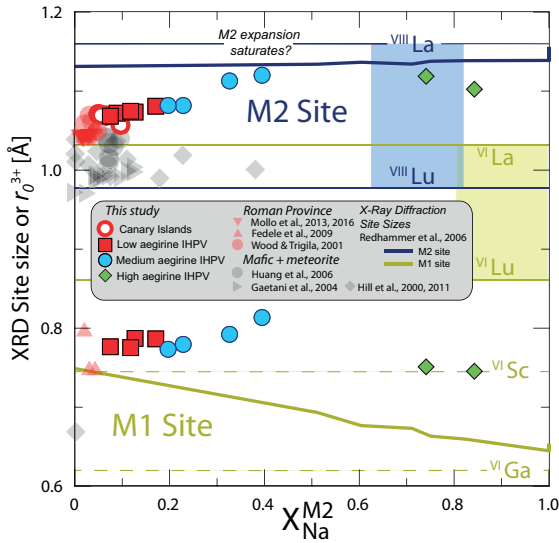


Figure 9: Diagram showing variation of ideal ionic radius r_0^{3+} with $X_{\text{Na}}M_2$ for M1 and M2 sites of clinopyroxene. Shown for comparison are single crystal x-ray diffraction data from the hedenbergite-aegirine compositional join (heavy solid lines, from Redhammer et al., 2006). Shaded boxes represent the range of ionic radii for rare earth elements in VI and VIII coordination (Shannon, 1976). Literature data for the Roman Province, Italy are from Fedele et al. (2009); Mollo et al. (2013, 2016); Wood and Trigila (2001) and for mafic systems are from Hill et al. (2000, 2011); Gaetani (2004); Huang et al. (2006).

ions in the T and M1 sites prevent further expansion of the M2 site as additional R_{M2}^{3+} is added to the clinopyroxene. For the M1 site of clinopyroxene, strain free radii for R^{3+} cations indicate expansion between low and medium-aegirine clinopyroxene and contraction between medium and high-aegirine clinopyroxene (Figs. 8, 9). These trends broadly follow the substitution of Mg^{2+} for Fe^{2+} , then Fe^{2+} for Fe^{3+} with increasing aegirine content in the clinopyroxene.

5.4.2. The effect of cation charge on the D_0 parameter

The D_0 parameter of the lattice-strain model describes ideal, strain-free partitioning and tracks the solubility of an ideal cation in the mineral with changing pressure, temperature and the bulk composition of the system (Wood and Blundy, 2014). D_0 therefore correlates with the major-element composition of the clinopyroxene. Moreover, incorporation of trace-elements of a different charge introduces an electrostatic penalty that leads to a lower D_0 for that charge (Wood and Blundy, 2001, 2003).

The average charge of major-elements on the M2 site of clinopyroxene decreases from 2+ to 1+ on the compositional join between Ca-rich diopside and Na-

rich aegirine. Consequently, the electrostatic penalty for substituting a REE^{3+} cation into the clinopyroxene M2 site is increased. Indeed, $D_{0,M2}^{3+}$ decreases as Ca exchanges for Na (Fig. 10e). Conversely, as the average charge on the M1 site of clinopyroxene increases from 2+ toward 3+ in end-member aegirine, the electrostatic penalty incurred when substituting REE^{3+} cations onto the M1 site is reduced (Fig. 10f). As a result, $D_{0,M1}^{3+}$ increases by approximately an order of magnitude between our medium-aegirine and high-aegirine experimental clinopyroxene, an effect that when combined with the shrinking M1 site size, leads to strong fractionation of the HREE (Figs. 8 and 10f).

A positive correlation between Al^T and partition coefficients for highly charged trace-elements has been extensively documented in studies on clinopyroxene (Lundstrom et al., 1994; Gaetani and Grove, 1995; Blundy et al., 1998; Francis and Minarik, 2008; Hill et al., 2011; Mollo et al., 2016). The low-aegirine experimental clinopyroxene and most of the Canary Islands rocks extend trends defined by clinopyroxene from mafic systems (Fig. 10a), whereas the remainder of the experimental data set and Canary Islands rocks show element-partitioning behaviour similar to the potassic Roman Province of Italy (Wood and Trigila, 2001; Fedele et al., 2009; Mollo et al., 2016), confirming that an Al^T -controlled substitution mechanism extends to peralkaline conditions (Figs. 7, 10a).

Tetrahedral Al is thought to facilitate incorporation of REE^{3+} cations onto the M2 site of clinopyroxene by replacing Si^{4+} , thereby reducing local charge and thus the electrostatic penalty associated with incorporation of REE (Blundy et al., 1998). The substitution of Fe^{3+} for tetrahedral Si^{4+} can be expected to have a similar effect. Conversely, R^{3+} ions on the neighbouring M1 site should hinder incorporation of REE on the M2 site, because they increase local charge by replacing R^{2+} ions, such as Mg^{2+} and Fe^{2+} . This electrostatic penalty should apply doubly to Ti^{4+} on the M1 site. This effect is consistent with our experimental data (Fig. 10c), but is not obvious in the natural samples, nor in the majority of the literature experimental data. It would thus appear that other factors, such as melt structure, have a stronger control on D_{REE} (e.g. Prowatke and Klemme, 2005).

D_0^{3+} parameters for the M1 site are strongly correlated with those for the M2 site, except at aegirine concentrations exceeding 50 mol.%. Similarities to M2 partitioning behaviour likely reflect the dominance of T-site substitution mechanisms in augite clinopyroxene. In the high-aegirine clinopyroxene, T-site substitutions become less important as the T-sites become saturated with Si^{4+} (Fig. 5). The replacement of Fe^{3+} at the

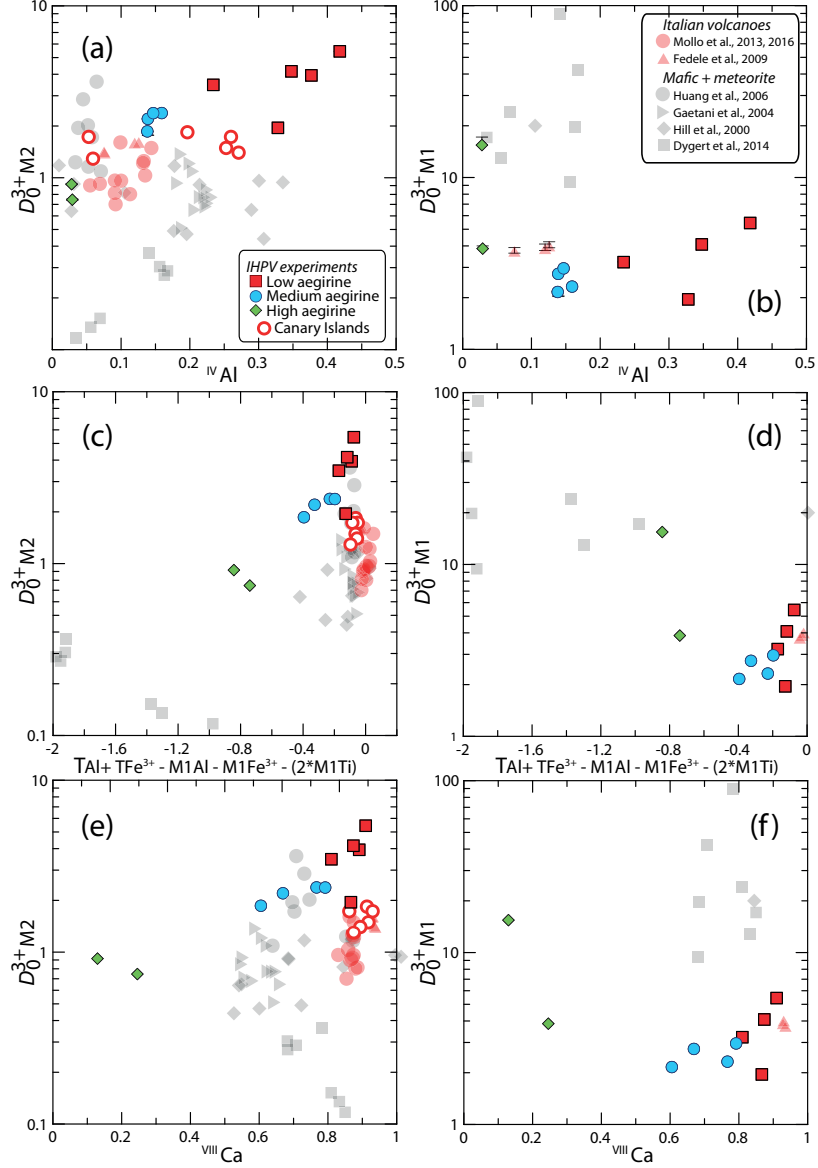


Figure 10: Strain-free partitioning coefficients (D_0) for 3+ ions into clinopyroxene vs. various charge compensation mechanisms. (a,c,e) are for the M2 site, and (b,d,f) are for the M1 site. The diagrams show that variability in partitioning behaviour is highly dependent on mineral composition, and that variation between aegirine-rich clinopyroxene cannot be explained well by the same mechanisms as more mafic systems. Literature data for element-partitioning in Mafic + Meteorite and Roman Province compositions are from the compilation of Bédard (2014). 1σ uncertainties are shown in (a, b) and are usually smaller than the symbol sizes.

961 M1 site by 3+ trace-elements does introduce a charge 1012
962 penalty, therefore D_{0M1}^{3+} increases accordingly. 1013

963 5.5. The effects of melt structure on element- 1015 964 partitioning 1016

965 The partitioning of trace-elements between crystals 1017
966 and melts is controlled by their relative activity in each 1018
967 phase and the exchange mechanisms by which their 1019
968 incorporation into crystals takes place (e.g., Jd-melt, 1020
969 Jd-DiHd and CaTS-DiHd exchanges have been shown 1021
970 to control REE incorporation in cpx, Putirka, 2008; 1022
971 Wood and Blundy, 2014; Mollo et al., 2017). As 1023
972 such, one might expect to see correlations between melt 1024
973 structural parameters and trace-element-partition 1025
974 coefficients. Such correlations have been reported by nu- 1026
975 merous authors (e.g., Schmidt et al., 2006; Mollo et al., 1026
976 2017), but appear to be expressed over a limited range 1027
977 of melt compositions (Gaetani, 2004; Huang et al., 1028
978 2006). A widely used descriptor for melt structure is 1029
979 the ratio of non-bonding oxygen anions to tetrahedrally- 1030
980 coordinated cations ($\frac{NBO}{T}$, Mysen et al., 1982, 1985). In 1031
981 relatively polymerised melts, where this ratio falls be- 1032
982 low 0.49, melt structure has been shown to have a sig- 1033
983 nificant influence on mineral–melt partition coefficients 1034
984 (Gaetani, 2004; Huang et al., 2006). 1035

985 To calculate NBO/T for our experiments, we es- 1036
986 timated melt Fe oxidation state from run tempera- 1037
987 tures and known fO_2 buffer conditions (Kress and 1038
988 Carmichael, 1991). The recalculated total of major- 1039
989 element oxides (incl. Fe_2O_3) was then used to approxi- 1040
990 mate the water content of the quenched melts. Oxygen 1041
991 from this dissolved water was added into the NBO/T 1042
992 calculation, which followed Mysen et al. (1985). The 1043
993 high content of alkalies and dissolved water in the 1044
994 experiments presented here produced melts that have 1045
995 $NBO/T = 0.98\text{--}1.42$; well above the compositional 1046
996 boundary reported by Gaetani (2004). Consistent with 1047
997 his findings, most trace-element-partition coefficients 1048
998 determined from our experiments are uncorrelated with 1049
999 the NBO/T ratio of the melt (Fig. 11). An exception is 1050
1000 $D_{S,r}$, that shows a weak positive correlation with NBO/T 1051
(Fig. 11c). NBO/T could not be calculate for our Ca- 1052
1002 Canary Islands compositions because the water content of 1053
1003 the melt prior to quench is not known. 1054

1004 Because partition coefficients between clinopyroxene 1055
1005 and melt are controlled by the relative activity of ele- 1056
1006 ments in each of these two phases, an empirical model 1057
1007 to predict partition coefficients from both melt and min- 1058
1008 eral compositional terms has the highest potential for 1059
1009 accuracy. Application of such a model would however 1060
1010 require measurement of both mineral and melt phases, 1061
1011 which would limit its geological utility. A similar model 1062

1012 based only on clinopyroxene composition could be ap-
1013 plied in a wider range of scenarios where melt compo-
1014 sition cannot be directly measured, for example to cumu-
1015 late systems or to concentrically zoned phenocrysts. Be-
1016 cause crystallisation is a thermodynamically controlled
1017 process, the composition of the melt and thus its effects
1018 on element-partitioning will, at least in part, be recorded
1019 by the composition of the clinopyroxene. This consid-
1020 ered, we chose to calibrate a clinopyroxene-based em-
1021 pirical partitioning model, based on lattice-strain the-
1022 ory that would be applicable over a wide compositional
1023 range from tholeiitic basalts to peralkaline phonolites.
1024 Details are provided in the following sections.

1025 5.6. An element-partitioning model extending to ae- 1026 1026 girine clinopyroxene

1027 Element partition coefficients vary systematically
1028 with the physiochemical conditions of natural and syn-
1029 synthetic magmas (cf. Wood and Blundy, 2003). Conse-
1030 quently, a host of models have been presented to de-
1031 scribe the systematics of element-partitioning between
1032 clinopyroxene and silicate melts (Wood and Blundy,
1033 1997, 2001; Hill et al., 2011; Yao et al., 2012; Sun and
1034 Liang, 2012; Bédard, 2014; Dygert et al., 2014; Mollo
1035 et al., 2016). The majority of these models are based on
1036 lattice-strain theory and predict how the lattice parame-
1037 ters r_0 , E_s , and D_0 vary with composition, temperature
1038 and pressure. This semi-thermodynamic approach theo-
1039 retically permits calculation of partition coefficients for
1040 any trace-element, at any set of $P - T - X$ conditions. In
1041 reality, all models have a limited working range, as re-
1042 stricted by the input data set. Because existing parti-
1043 tioning models do not reproduce the high $r_{0,M2}^{3+}$ values for
1044 clinopyroxene with aegirine contents ≥ 50 mol % (Fig.
1045 12a), they cannot accurately predict REE partitioning
1046 behaviour for strongly peralkaline systems. Here, we
1047 present a new empirical model that is calibrated on both
1048 our experimental work and natural partition coefficients
1049 from Canary Islands rocks, as well as existing parti-
1050 tioning data from the literature (compilation of Bédard,
1051 2014, Fig. 12, Table S1).

1052 Our model focuses on the dependence of element-
1053 partitioning on clinopyroxene composition, temperature
1054 and pressure only. While partition coefficients are ther-
1055 modynamically controlled by activity of elements in
1056 both the crystal and the melt phase (Wood and Blundy,
1057 2014), and while melt structure has been shown to influ-
1058 ence element-partitioning (Huang et al., 2006; Schmidt
1059 et al., 2006; Mollo et al., 2017), it is not always pos-
1060 sible to measure melt composition directly. For ex-
1061 ample, equilibrium melt compositions cannot be mea-
1062 sured for the cores of zoned clinopyroxene phenocrysts

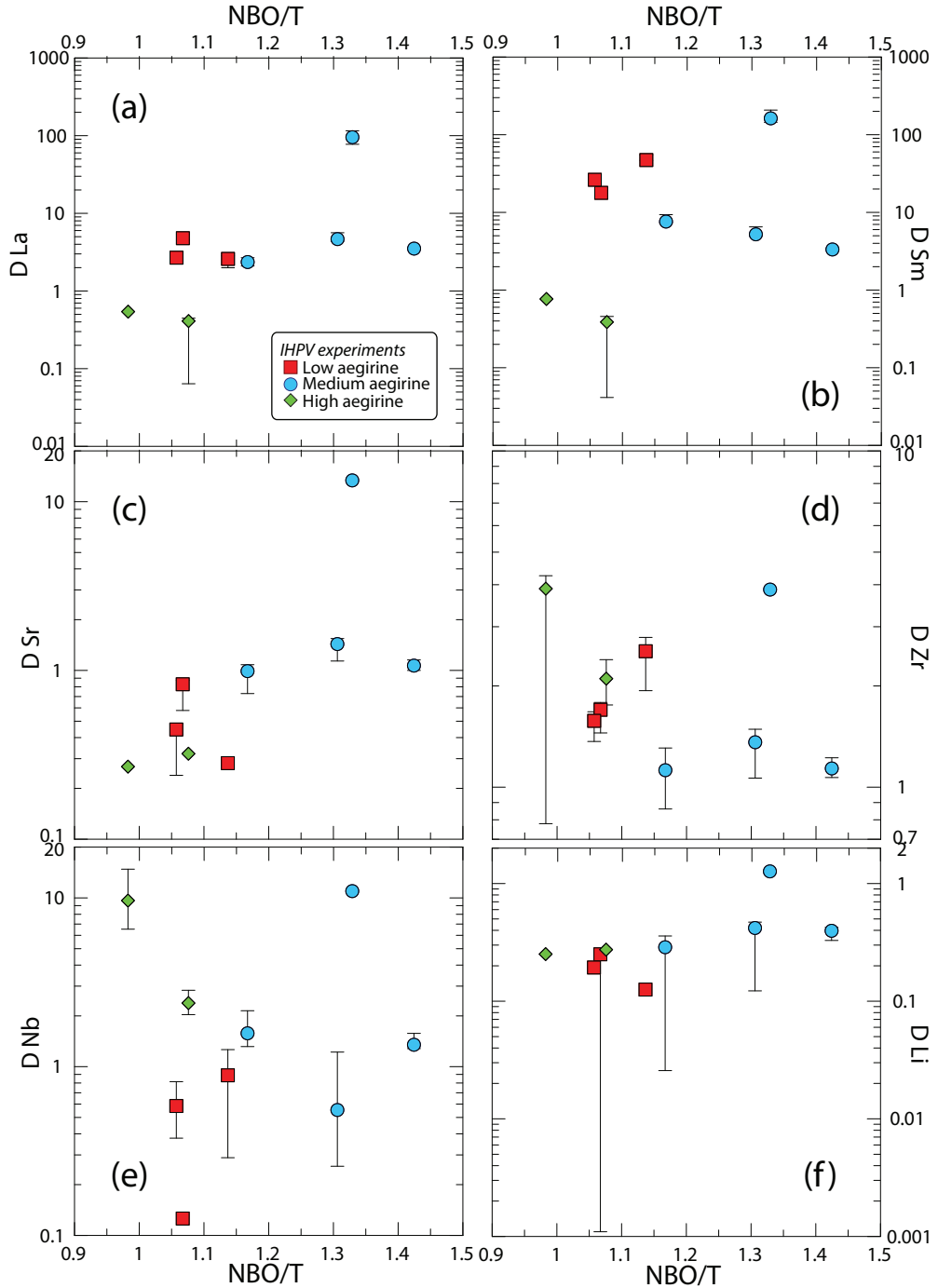


Figure 11: Diagrams of clinopyroxene–melt trace-element-partition coefficients for the IHPV experiments as a function of NBO/T of the quenched melt (Mysen et al., 1985). The water-saturated, sodic compositions investigated produce melts with highly depolymerised structures. The NBO/T ratio of these melts is not correlated with trace-element-partition coefficients, except weakly in the case of Sr. In highly polymerised systems ($\text{NBO}/\text{T} < 0.49$, Gaetani 2004) partition coefficients for REE and HFSE are negatively correlated with this parameter. (see Fig. 9 from Huang et al. 2006).

in tephra, or indeed for any crystal from an intrusion in which gravitational segregation of phases has occurred. Therefore, while the predictive power of a model based only on the compositions of the crystal should be lower than that of a model based on both crystal and melt compositions, a crystal-only model may be applied to a wider spectrum of geological scenarios. Melt composition should, at least in part, be recorded by the major-element composition of the clinopyroxene.

5.6.1. The clinopyroxene M2 site

To find the principal physiochemical factors that affect element-partitioning at the M2 site of clinopyroxene, a stepwise least-squares multiple linear regression analysis was performed using the lattice-strain parameters r_0^{3+} , E_s^{3+} and D_0^{3+} , temperature, pressure and clinopyroxene composition as inputs. Input parameters were initially examined in binary scatter diagrams to ascertain whether correlations with lattice-strain parameters were linear. If not, interaction compositional terms were added to the initial set of possible fitting parameters that had linear correlations with lattice-strain parameters (e.g. $X_{Al+Fe^{3+}}^T$). Intensive variables for multiple regression models for r_0 , E_s and D_0 were introduced following a hierarchical forward selection criterion with switching. The largest number of significant terms to describe a lattice-strain parameter was eight for E^{M2} (c.95%, cf. Supplement S4).

Because of systematic covariation of compositional parameters in our small data set of experiments and natural samples ($n = 16$), a model calibrated with these points alone would be unable to deconvolve the effects of each major-element on partitioning behaviour. We have therefore added published experiments and natural phenocryst-glass pairs ($n = 75$) to assemble a database covering a wide range of composition, pressure, temperature and oxygen fugacity (data from compilation of Bédard 2014, and Mollo et al. 2016, 0.0001–3.5 GPa, 650–1345 °C, $\log fO_2 = IW$ to MH $\approx \Delta QFM - 5$ to +5). clinopyroxene compositions cover XMg 0.031–1, X_{Na}^{M2} 0–0.84 and Al^T 0–0.49 c.f.u. and melt compositions vary widely in terms of Mg# (0–100) and XH_2O (0–0.38). REE partition coefficients also vary significantly (e.g. D_{La} 0.01–4.79; D_{Sm} 0.02–47.24, and D_{Yb} 0.11–8.00). The majority of partition coefficients in the training data set were measured via SIMS or LA-ICP-MS, minimising analytical uncertainty (e.g. from analyses by electron-microprobe).

The resultant empirical model accounts well for changes in lattice-strain parameters over a range of compositions from basalt to peralkaline phonolite, faithfully reproducing large r_0^{M2} values typical for sodic

clinopyroxene (Fig. 12, model coefficients in Table 5). Student t-tests show that all of the independent variables included in the models are significant at the 95% confidence level and PRESS R^2 values were obtained by repeated by randomly subsampling the dataset (Stevens, 1996), are close to R^2 values calculated by regular methods, indicating robust models with high predictive power. Full multiple regression reports are available in Supplement S4. Equations generated by the multiple linear regression calculations are given below for the M2 site, where a_i are the regression coefficients for the respective variables:

$$\ln D_0^{M2} = a_1 + a_2 T + a_3 X_{Al+Fe^{3+}}^T + a_4 X_{Ti}^{M1} + a_5 X_{Al-Fe^{3+}}^{M1} + a_6 X_{Fe^{2+}}^{M2} \quad (3)$$

$$E^{M2} = a_7 + a_8 P + a_9 X_{Al+Fe^{3+}}^T + a_{10} X_{Al}^{M1} + a_{11} X_{Mg}^{M1} + a_{12} X_{Ti}^{M1} \\ + a_{13} X_{Mg}^{M2} + a_{14} X_{Mg} \quad (4)$$

$$r_0^{M2} = a_{15} + a_{16} T + a_{17} X_{Al-Fe^{3+}}^{M1} + a_{18} X_{Ti}^{M1} + a_{19} X_{Ca}^{M2} + a_{20} X_{Na}^{M2} \quad (5)$$

The model for r_0^{M2} is robust with high predictive power and incorporates compositional controls from the M1 and M2 sites, as well as temperature. Elevated concentrations of large M2 cations Ca²⁺ and Na⁺ are correlated with large M2 sites. Ti⁴⁺ cations in the neighbouring M1 site are also correlated with expansion of the M2 site, and the concentration of small Al³⁺ minus larger Fe³⁺ on the M1 site is negatively correlated with r_0^{M2} . The negative correlation between r_0^{M2} and temperature reflects the sum of changes to major-element composition that lead to smaller clinopyroxene M2 sites at higher temperatures. This compositional effect swamps the minor influence of thermal expansion.

D_0^{M2} is reasonably well predicted and incorporates compositional terms from all three sites in clinopyroxene and temperature. The positive effect of tetrahedral R³⁺ on D_0^{M2} is the largest contribution to the model, which is consistent with published studies (see above). The relationship between clinopyroxene compositional terms on the M1 and M2 sites and D_0 are indirect and are tied to the solubility of the mineral in the melt (Wood and Blundy, 2003), which in turn is tied to the physiochemical conditions of the system (largely melt composition). The model for D_0^{M2} is less robust than

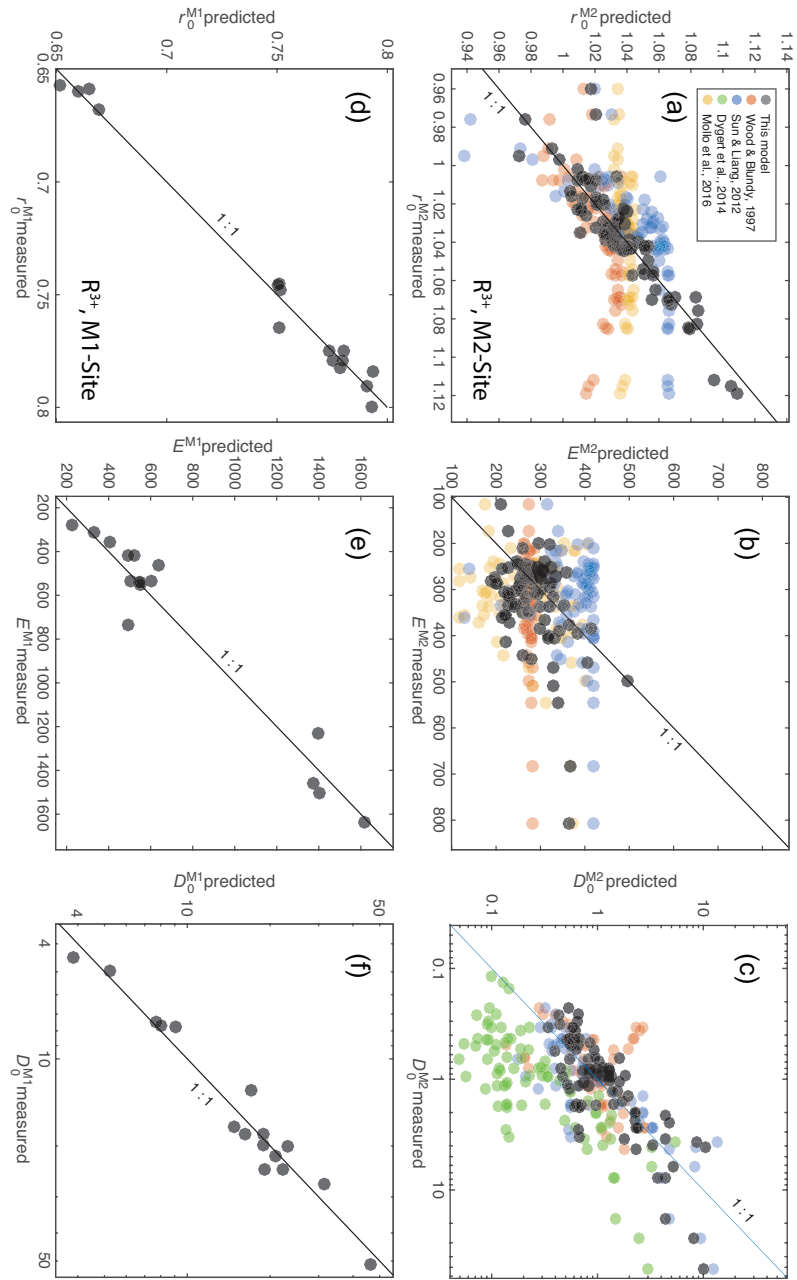


Figure 12: Measured vs. predicted model values for lattice-strain parameters for the M2 and M1 sites of clinopyroxene. The new models presented here were generated via a stepwise multiple linear regression procedure following a hierarchical forward selection criterion with switching. Full regression reports are in Supplement S4 and model equations are in the main text.

1151 that for r_0^{M2} , largely because there are melt compositional effects that are not recorded in the composition of the clinopyroxene. We tested the Mg# and XH_2O of the melt, neither of which are significant predictors for D_0^{M2} .

1152 The model for E^{M2} is less well-constrained than for the other two M2 lattice-strain parameters, suggesting that M2 site stiffness is not tied strongly to clinopyroxene composition, temperature or pressure. Despite a significantly lower predictive power, this model still has physical grounding. Stiffness of the M2 site is positively correlated with pressure, as might be expected following a simple Hooke's law relationship, and there are some subtle compositional controls imparted by the T and M1 sites. The poor correlation between E^{M2} , clinopyroxene composition, temperature and pressure is also evident in published element-partitioning models, where E^{M2} is either poorly predicted (Fig. 12b), or set to a fixed value (e.g. Dygert et al., 2014).

1153 Diagrams of measured vs. predicted D values for R³⁺ cations are given in Figure 13a, showing the predictive power of the models over a compositional range between basalt and peralkaline phonolite. For the M2 site, 95% of the measured R³⁺ partition coefficients are reproduced within a factor of $\frac{+2.5}{-2.9}$ (hard dashed lines), and in extreme cases, the model still reproduces D values within an order of magnitude, sufficient for the prediction of element-partitioning trends over a wide range of $P - T - X$. D_{MREE} , such as Sm, are reproduced more faithfully than D_{LREE} , because their radius is closer to r_0^{M2} (Fig. 13c,d), and therefore prediction of their partitioning behaviour is affected less strongly by inaccuracies in predicted E^{M2} values.

1154 5.6.2. The clinopyroxene M1 site

1155 Using a methodology similar to the M2 site, we fitted a predictive model for partitioning of R³⁺ cations onto the smaller, 6-coordinated M1 site of clinopyroxene. Lattice-strain parabola were constrained by partitioning data for Cr, Ga, Sc, and where suitable, the HREE Tm, Yb and Lu (Our IHPV experiments plus Hill et al. 2000; Fedele et al. 2009; Mollo et al. 2013; Dygert et al. 2014). The training data set for the M1 site partitioning model is small relative to that for the M2 site ($n = 18$), and because it is strongly skewed toward alkali compositions, it has lower predictive power and is not recommended for application to mafic magmatic systems. Equations for the M1 site lattice-strain parameters, as generated by multiple linear least squares regression, are given below and shown in Figure 12 where b_i are the regression coefficients (Table 5) for the respective variables:

$$lnD_0^{M1} = b_1 + b_2X_{Al}^T + b_3X_{Fe^{2+}}^{M1} + b_4X_{Ca}^{M2} + b_5X_{Na}^{M2} \quad (6)$$

$$E^{M1} = b_6 + b_7T + b_8P + b_9X_{Mg}^{M1} \quad (7)$$

$$r_0^{M1} = b_{10} + b_{11}P + b_{12}X_{Mg}^{M2} + b_{13}X_{Fe^{2+}}^{M1} + b_{14}X_{Ca}^{M2} \quad (8)$$

The model for r_0^{M1} is robust and accurately reproduces the input data set. A negative pressure term may reflect compressional strain on the crystal lattice. Large Fe³⁺ cations have a positive effect on the size of the M1 site, while smaller Mg²⁺ cations on the neighbouring M2 site have a negative effect on M1 site size. The small negative X_{Ca}^{M2} term is indirectly related to the size of the M1 site.

E^{M1} is predicted more accurately than E^{M2} and is largely described by variations in temperature and pressure. Much like the M2 site, stiffness of the M1 site appears to be controlled dominantly by physicochemical factors that are not recorded in the composition of the clinopyroxene.

The model for D_0^{M1} contains compositional terms from all three crystallographic sites in clinopyroxene. X_{Al}^T has a strong positive correlation with D_0^{M1} , consistent with a charge compensation mechanism that aids incorporation of R³⁺ cations, while terms for M1 and M2 site cations may be indirectly recording melt compositional effects. Because D_0^{M1} is unusually high for our high-aegirine experiments, they had to be excluded from the fitting procedure to permit model convergence. The models for r_0^{M1} and E^{M1} are calibrated for use all the way to end-member aegirine, but this was not possible for the D_0^{M1} term, which is calibrated for use up to $\sim Ae_{50}$. Further experiments at conditions between those that generated our medium and high-aegirine clinopyroxene would be required to better constrain the clinopyroxene compositional record of D_0^{M1} in strongly peralkaline Fe-rich magmas.

When applied to our experimental data, and the compilation of partition coefficients from the Roman Province (Fedele et al., 2009; Mollo et al., 2013, 2016), the M1 stepwise model reproduces element-partitioning data to a factor of $\frac{+7}{-11}$ at the 95% confidence interval (Fig. 13b). Full regression reports are provided in Supplement S4.

For convenience, we provide an EXCEL spreadsheet for calculation of clinopyroxene-melt element-partition coefficients for any trace-element of 3+ valence that is

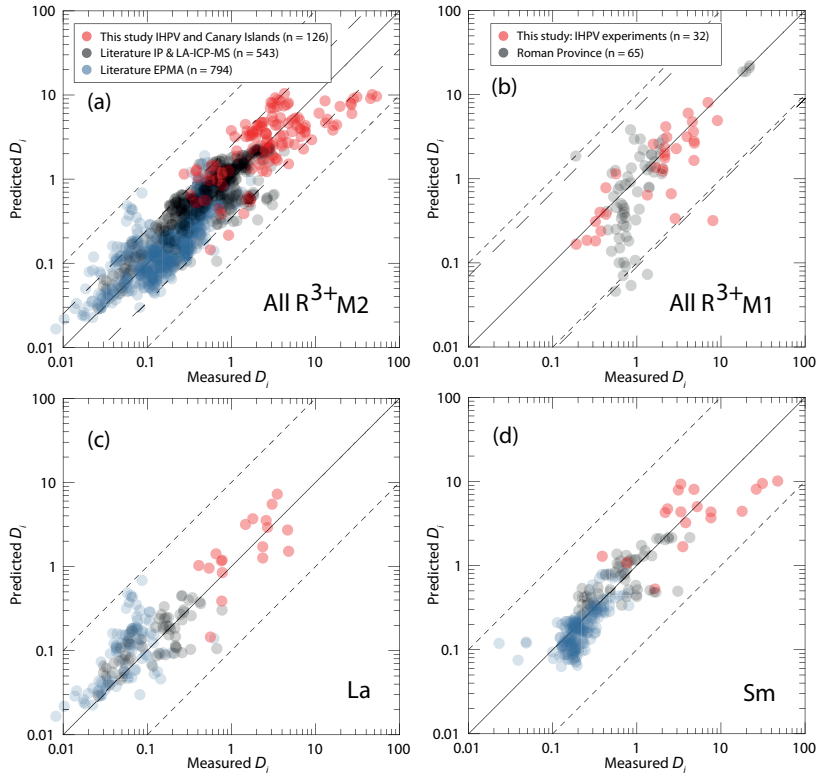


Figure 13: Measured clinopyroxene–silicate melt partition coefficients for 3+ cations vs. those predicted by our empirical model. (a) shows a comparison between measured partition coefficients and model-derived values for the M2 site of clinopyroxene. Hard dashed lines represent 95% confidence intervals of the model, and correspond to maximum uncertainties of factor $\frac{+2.5}{-2.5}$. Fine dashed lines represent 1 order of magnitude uncertainty (extreme outliers for M2 model). Partition coefficients in this diagram are the REE La to Er for our IHPV experiments, Canary Islands rocks, and literature data from the Roman Province (Wood and Trigila, 2001; Fedele et al., 2009; Mollo et al., 2013, 2016), and all the REE plus Y for the rest of the data compilation (Bédard, 2014), which is split by analytical methodology. (b) shows performance of the predictive model for the M1 site that is calibrated for alkaline magmatic systems, and includes data from our IHPV experiments and the Roman Province (Fedele et al., 2009; Mollo et al., 2013, 2016). Maximum uncertainties at the 95% confidence interval are a factor of $\frac{+7}{-11}$, higher than for the M2 site because of the smaller calibrating data set. (c) performance of the M2 site model for La, and (d) for Sm.

large enough to fit onto the M1 or M2 sites of clinopyroxene (Supplement S5). To assess the utility of the partitioning models and to monitor for potential introduction of radius-dependent bias, we show predicted REE patterns normalised to measured ratios for some literature data and our internally heated pressure vessel experiments (Fig. 14). The model accurately reproduces REE patterns at all compositions, except for HREE on the M1 site of clinopyroxene at aegirine contents exceeding ~50 mol% (NLS experiments).

5.7. Implications for formation of REE deposits in evolved alkaline intrusions

The solubility of REE and HFSE minerals is strongly enhanced in peralkaline melts (Watson, 1979; Linnen and Keppler, 1997; Boehnke et al., 2013; Asperi et al., 2015), thus the high concentration of these elements

in peralkaline systems may (partially) reflect this fact (Dostal, 2017). Melts containing high concentrations of REE and HFSE are thought to be generated through low degrees of partial melting in the source, followed by residual enrichment during protracted fractional crystallisation (Marks and Markl, 2017). The budget of REE and HFSE in a fractionating magma is influenced by the mineralogy of the crystallising assemblage, and the extent to which these elements are incorporated at minor or trace concentrations.

Pyroxene is a major ferromagnesian phase that is commonly saturated throughout the entire differentiation histories of peralkaline magmatic systems (Ablay et al., 1998; Marks and Markl, 2001; Möller and Williams-Jones, 2016). The composition of the fractionating clinopyroxene has a major impact on the absolute REE concentrations and REE pattern of the residual

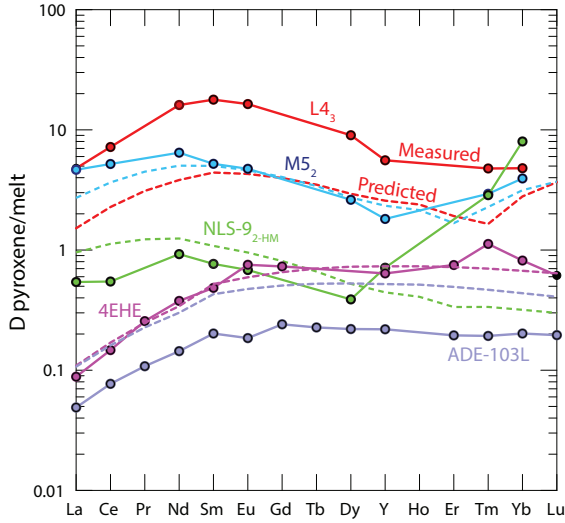


Figure 14: Measured and predicted element-partition coefficients for REE^{3+} . The model does not introduce notable radius-dependent biases, except for in our high-aegirine clinopyroxene (NLS-9_{2-HM} in green) for which D_{HREE} are strongly underpredicted, owing to inaccurate return of D_0^{M1} . Shown for comparison are two diopside–melt pairs: 4EHE from Hill et al. (2000), grown from a synthetic (NC-MAS) basaltic andesite composition and ADE-103L from Lofgren et al. (2006) grown from a picritic composition based on the Angra dos Reis meteorite.

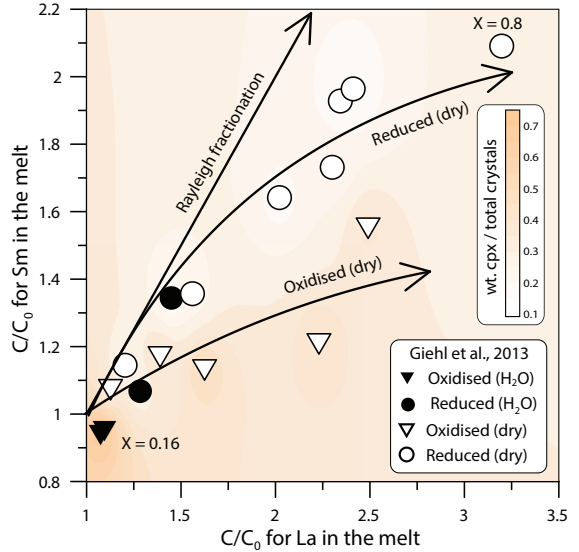


Figure 15: Model enrichment paths for La and Sm in residual melts during fractional crystallisation of a MiKa dyke composition (Gardar Province, Greenland, see Marks and Markl 2003). Phase relations and clinopyroxene compositions are from Giehl et al. (2013) and pertain to both oxidising and reducing conditions ($\log f\text{O}_2 = \Delta\text{QFM} - 3$ and +1), nominally dry to water bearing (to 3 wt.% H_2O at 1 kbar). Colour shading indicates the weight fraction of clinopyroxene within the crystallising assemblage. Bold arrows indicate residual enrichment pathways for the REE in the melt for Rayleigh fractionation (no incorporation into crystals), reduced, dry conditions, and oxidised dry conditions (the latter two are hand drawn fits to the data). For simplicity, this model does not consider REE incorporation into magnetite, alkali-feldspar, olivine, nepheline or aenigmatite, all phases generated in the experiments of Giehl et al. (2013) (see Larsen, 1979; Kovalenko et al., 1988; Mahood and Stimac, 1990).

melt, and ultimately on the ability of a system to develop economic concentrations of the REE (Fig. 15, e.g. Kogarko, 1990; Sørensen, 1992; Marks et al., 2011). Pyroxene in alkaline magmatic systems is initially calcic for mafic melts, and becomes increasingly sodic as crystal fractionation proceeds (Marks et al., 2004). Although the REE are compatible in the majority of our experimentally generated clinopyroxene, those approaching aegirine end-member composition, as found in evolved alkaline magmatic systems have the lowest D_{REE} values (Fig. 6). Strongly alkaline magmatic systems are thought to crystallise abundant Ca-pyroxene early in their evolution which may deplete residual liquids with respect to REEs. Consequently, even though crystallisation of Na-pyroxene could enrich residual liquids with REE, the resultant concentration of these metals in the melt would remain low. However, clinopyroxene is not the only phase to crystallise from alkaline magmas, and the majority of additional silicate phases, such as olivine, biotite and feldspar have $D_{\text{REE}} \ll 1$, typically 1-4 orders of magnitude lower than clinopyroxene (Larsen, 1979; Kovalenko et al., 1988; Mahood and Stimac, 1990). Consequently, if the mode of clinopyroxene is low enough, the bulk D_{REE} of the crystallising assemblage would remain below unity, allowing the

REE to become enriched in the residual silicate melt.

To give insight into the optimum conditions for residual magmatic enrichment of the REE in alkaline systems we modelled the evolution of REE concentrations in the melt during fractional crystallisation of a nepheline syenite body (Fig. 15). Phase relation data and clinopyroxene compositions are from the experimental study of Giehl et al. (2013). Their starting composition, based on the MiKa dyke, from the Gardar Province, Greenland, is already extremely evolved, with $\text{Mg}\# = 2$, $(\text{Na} + \text{K})/\text{Al} = 1.44$ and $\text{FeO}^* = 12$ wt.%.

In these models, crystallisation under water-bearing, oxidising conditions produces a high fraction of clinopyroxene that depletes residual melts with respect to Sm, while subtly enriching La. Dry conditions promote abundant alkali feldspar (Afs) crystallisation, which effectively enriches the REE content of residual melts. Under oxidising, dry conditions, the La/Sm ratio of the residual melt increases with fractionation, be-

cause Sm is more effectively incorporated into clinopyroxene. Residual enrichment is most effective under dry, reducing conditions because of a relatively lower fraction of clinopyroxene within the crystallising assemblage. Because of this, the REE enrichment path of the residual melt is close to that of ideal Rayleigh fractionation. Under these reducing, dry conditions and at a temperature of 750°C, the experiments of Giehl et al. (2013) attained a crystal fraction of 0.8. Here, residual melts would have 3.2 times La concentration and 2 times the Sm concentration relative to their starting composition.

Considering these mechanisms, alongside our experimental and Canary Islands data, the best systems to develop high REE concentrations are those that would produce small proportions of Ca-pyroxene early in their crystallisation histories, quickly evolving to more sodic compositions that crystallise aegirine clinopyroxene. Cooling under low-pressure, dry, reducing conditions produces abundant alkali feldspar that in the case of a peralkaline composition, would serve to further increase the alkalinity of the residual melt. Low degrees of source melting would produce primary melts with (1) high REE concentrations and (2) low melt Mg + Fe, and low modal abundance of clinopyroxene, which would aid enrichment in residual melts via fractional crystallisation.

The HREE-rich nature of peralkaline magmatic systems, both granites and nepheline syenites, is compatible with fractionation of moderately sodic clinopyroxene that have high D_{LREE}/D_{HREE} (e.g. Möller and Williams-Jones, 2016; Dostal, 2017). As crystal fractionation progresses and clinopyroxene compositions evolve toward the aegirine end-member composition, D_{LREE}/D_{HREE} decreases (Fig. 6). This systematic change in element-partitioning behaviour would result in strong HREE enrichment in aegirine-pyroxene cumulates, and would enrich the residual melt with respect to LREE-MREE.

Conclusions

- Our experiments reveal three distinct element-partitioning behaviours for Na-rich clinopyroxene that depend on aegirine content. Each of these is associated with a distinct major-element exchange vector. We do not have the compositional resolution to know if the transition between these behaviours is smooth or step-like.
- Fits to the lattice-strain model of Blundy and Wood (1994) indicate expansion of the M2 site with increasing Na_{M2}⁺, to a maximum $r_{0,M2}^{3+}$ of 1.12 Å at Na_{M2}⁺ = 0.4 c.f.u. Further expansion did not occur at higher Na contents.

creasing Na_{M2}⁺, to a maximum $r_{0,M2}^{3+}$ of 1.12 Å at Na_{M2}⁺ = 0.4 c.f.u. Further expansion did not occur at higher Na contents.

- Both the M1 and M2 sites shrink at high-aegirine contents in response to increasing ΣR_{M1}^{3+} .
- Charge effects lead to a progressive increase in D_0^{M1} at the expense of D_0^{M2} , as the exchanges Ca²⁺ for Na⁺ and M²⁺ for Fe³⁺ take place. Much like in systems of lower alkalinity, REE incorporation into clinopyroxene is dominated by coupled Al-Si substitutions at the T-site.
- Existing predictive models for clinopyroxene/melt element-partitioning do not accurately reproduce the large M2 site ($r_{0,M2}^{3+}$) of clinopyroxene with aegirine content exceeding 50 mol%. We have calibrated a new empirical model that may be applied to any composition between basalt and peralkaline phonolite, based on our data from experiments and natural systems, as well as a large compilation of partition coefficients from the literature.
- Crystallisation of abundant Ca-Mg rich clinopyroxene depletes the residual melts of REE, and inhibits or terminates magmatic enrichment processes.
- Element partitioning systematics suggest that nepheline syenites which host REE deposits must originate from low-degree melts with sufficient alkali enrichment to saturate clinopyroxene similar to our medium-aegirine clinopyroxene (Ae_{25–50}). Fractionation of such clinopyroxene enriches residual melts with respect to the HREE, in accord with the composition of REE-mineralised nepheline syenite systems.

Acknowledgements

We thank the Geo.X partners GFZ and Universität Potsdam for access to the HP-GeoMatS Lab, Don Baker for assistance with preparation of starting materials, Bruce Watson and Volker Möller for providing samples of Mud Tank zircon and the Nechalacho rocks, respectively, Hans Peter Nabein, Maria Stuff and Julia Pohlenz for assistance with HP experimental equipment, Toby Soutar for help with preparation of the Canary Islands samples, Lang Shi and Glenn Poirier for assistance with electron-microprobe analyses, and Anna Jung for assistance with laser ICP-MS analyses. The manuscript benefited from discussions with Longbo Yang, Rebecca

1415 Paisley, Shane Rooyakkers and Jean Bédard. Silvio 1474
 1416 Mollo, Lorenzo Fedele and an anonymous reviewer are 1475
 1417 thanked for their insightful feedback. Nelson Eby is 1476
 1418 thanked for editorial handling. This work was funded by 1477
 1419 PhD scholarships to C.B. from Geotop, DIVEX, and the 1478
 1420 SEG Canada Foundation, and operating grants to V.vH. 1479
 1421 and J.S. from the Natural Sciences and Engineering Re- 1480
 1422 search Council of Canada (grant numbers RGPIN-2014- 1481
 1423 05955, RGPAS-462335-2014) and the FQRNT team re- 1482
 1424 search project program. 1483

1425 References

- 1426 Ablay, G.J., Carroll, M.R., Palmer, M.R., Martí, J., Sparks, R.S.J., 1491
 1427 1998. Basanite–phonolite lineages of the Teide–Pico Viejo 1492
 1428 volcanic complex, Tenerife, Canary Islands. *Journal of Petrology* 39, 1493
 1429 905–936. doi:10.1093/petroj/39.5.905.
 1430 Ablay, G.J., Ernst, G.G.J., Martí, J., Sparks, R.S.J., 1995. The 2 ka 1494
 1431 subplinian eruption of Montaña Blanca, Tenerife. *Bulletin of Vol- 1495
 1432 canology* 57, 337–355. doi:10.1007/BF00301292.
 1433 Adam, J., Green, T., 2006. Trace element partitioning between mica- 1496
 1434 and amphibole-bearing garnet lherzolite and hydrous basanitic 1497
 1435 melt: 1. Experimental results and the investigation of controls on 1498
 1436 partitioning behaviour. *Contributions to Mineralogy and Petrology* 1499
 1437 152, 1–17. doi:10.1007/s00410-006-0085-4.
 1438 Akasaka, M., Onuma, K., 1980. The join CaMgSi₂O₆–CaFeAlSiO₆ 1500
 1439 –CaTiAl₂O₆ and its bearing on the Ti-rich fassaitic pyrox- 1501
 1440 enes. *Contributions to Mineralogy and Petrology* 71, 301–312. 1502
 1441 doi:10.1007/BF00371672.
 1442 Albert, H., Costa, F., Martí, J., 2015. Timing of magmatic pro- 1503
 1443 cesses and unrest associated with mafic historical monogenetic 1504
 1444 eruptions in Tenerife Island. *Journal of Petrology* 56, 1945–1966. 1505
 1445 doi:10.1093/petrology/egv058.
 1446 Andújar, J., Scaillet, B., 2012. Experimental constraints on parame- 1506
 1447 ters controlling the difference in the eruptive dynamics of phonolitic 1507
 1448 magmas: the case of Tenerife (Canary Islands). *Journal of Petrology* 53, 1777–1806. doi:10.1093/petrology/egs033.
 1449 Aseri, A.A., Linnen, R.L., Che, X.D., Thibault, Y., Holtz, F., 2015. 1508
 1450 Effects of fluorine on the solubilities of Nb, Ta, Zr and Hf minerals 1509
 1451 in highly fluxed water-saturated haplogranitic melts. *Ore Geology 1510
 1452 Reviews* 64, 736–746. doi:10.1016/j.oregeorev.2014.02.014.
 1453 Beard, C.D., 2018. Mineral–melt trace element partitioning in alkali- 1511
 1454 line magmatic systems. Phd thesis. McGill University, Montreal, 1512
 1455 Canada.
 1456 Bédard, J.H., 2014. Parameterizations of calcic clinopyroxene – Melt 1513
 1457 trace element partition coefficients. *Geochemistry, Geophysics, 1514
 1458 Geosystems* 15, 303–336. doi:10.1002/2013GC005112.
 1459 Behrens, H., Hahn, M., 2009. Trace element diffusion and viscous 1515
 1460 flow in potassium-rich trachytic and phonolitic melts. *Chemical 1516
 1461 Geology* 259, 63–77. doi:10.1016/j.chemgeo.2008.10.014.
 1462 Berndt, J., Liebske, C., Holtz, F., Freise, M., Nowak, M., Ziegen- 1517
 1463 bein, D., Hurkuck, W., Koepke, J., 2002. A combined rapid- 1518
 1464 quench and H₂-membrane setup for internally heated pres- 1519
 1465 sure vessels: description and application for water solubil- 1520
 1466 ity in basaltic melts. *American Mineralogist* 87, 1717–1726. 1521
 1467 doi:10.1029/JB089iB10p08540.
 1468 Blundy, J., Wood, B., 1994. Prediction of crystal–melt parti- 1522
 1469 tion coefficients from elastic moduli. *Nature* 372, 452–454. 1523
 1470 doi:10.1038/372452a0.
 1471 Blundy, J.D., Robinson, J.A.C., Wood, B.J., 1998. Heavy REE are 1524
 1472 compatible in clinopyroxene on the spinel lherzolite solidus. *Earth 1525
 1473 and Planetary Science Letters* 160, 493–504. doi:10.1016/S0012- 1526
 821X(98)00106-X.
 1475 Boehnke, P., Watson, E.B., Trail, D., Harrison, T.M., Schmitt, A.K., 1527
 1476 2013. Zircon saturation re-revisited. *Chemical Geology* 351, 324– 1528
 1477 334. doi:10.1016/j.chemgeo.2013.05.028.
 1478 Borchart, M., Wilke, M., Schmidt, C., Cauzid, J., Tucoulou, R., 2010. 1529
 1479 Partitioning of Ba, La, Yb and Y between haplogranitic melts and 1530
 1480 aqueous solutions: An experimental study. *Chemical Geology* 276, 1531
 1481 225–240. doi:10.1016/j.chemgeo.2010.06.009.
 1482 Boudreau, A.E., 2004. PALLADIUM, a program to model the 1532
 1483 chromatographic separation of the platinum-group elements, base 1533
 1484 metals and sulfur in a solidifying pile of igneous crystals. *Canadian 1534
 1485 Mineralogist* 42, 393–403. doi:10.2113/gscanmin.42.2.393.
 1486 Brown, R.J., Barry, T.L., Branney, M.J., Pringle, M.S., Bryan, S.E., 1535
 1487 2003. The Quaternary pyroclastic succession of southeast Tenerife, 1536
 1488 Canary Islands: explosive eruptions, related caldera subsidence, 1537
 1489 and sector collapse. *Geological Magazine* 140, 265–288. 1538
 1490 doi:10.1017/S0016756802007252.
 1491 Bryan, S.E., Martí, J., Cas, R.A.F., 1998. Stratigraphy of the Bandas 1539
 1492 del Sur Formation: an extracaldera record of Quaternary phonolitic 1540
 1493 explosive eruptions from the Las Cañadas edifice, Tenerife (Canary 1541
 1494 Islands). *Geological Magazine* 135, 605–636. doi:null.
 1495 Carracedo, J.C., Badiola, E.R., Guillou, H., Paterné, M., Scaillet, S., 1542
 1496 Torrado, F.J.P., Paris, R., Fra-Paleo, U., Hansen, A., 2007. Eruptive 1543
 1497 and structural history of Teide Volcano and rift zones of Tenerife, 1544
 1498 Canary Islands. *Geological Society of America Bulletin* 119, 1545
 1499 1027–1051. doi:10.1130/B26087.1.
 1500 Carroll, M.R., Blank, J.G., 1997. The solubility of H₂O in 1501
 1501 phonolitic melts. *American Mineralogist* 82, 549–556. 1502
 1502 doi:10.1093/petrology/32.5.1021.
 1503 Chou, I.M., 1986. Permeability of precious metals to hydrogen at 2 1504
 1504 kb total pressure and elevated temperatures. *American Journal of 1505
 1505 Science* 286, 638–658.
 1506 Corgne, A., Wood, B.J., 2005. Trace element partitioning and substi- 1507
 1507 tution mechanisms in calcium perovskites. *Contributions to Miner- 1508
 1508 alogy and Petrology* 149, 85–97. doi:10.1007/s00410-004-0638-3.
 1509 Costa, F., Chakraborty, S., Dohmen, R., 2003. Diffusion coupling 1509
 1510 between major and trace elements and a model for the calculation 1510
 1511 of magma chamber residence times using plagioclase. *Geochimica et 1511
 1512 Cosmochimica Acta* 67, 2189–2200. doi:10.1016/S0016- 1512
 7037(00)01345-5.
 1513 Coumans, J.P., Stix, J., Clague, D.A., Minarik, W.G., Layne, G.D., 1513
 1514 2016. Melt–rock interaction near the Moho: Evidence from crystal 1515
 1515 cargo in lavas from near-ridge seamounts. *Geochimica et Cos- 1516
 1516 mochimica Acta* 191, 139–164. doi:10.1016/j.gca.2016.07.017.
 1517 Deer, W.A., Howie, R.A., Zussman, J., 1992. An introduction to the 1517
 1518 rock-forming minerals. Longman Group Ltd, New York.
 1519 Dostal, J., 2017. Rare earth element deposits of alkaline igneous 1519
 1520 rocks. *Resources* 6, 1–12. doi:10.3390/resources6030034.
 1521 Downes, H., Balaganskaya, E., Beard, A., Lifervich, R., Demaiffe, 1520
 1521 D., 2005. Petrogenetic processes in the ultramafic, alkaline and 1521
 1522 carbonatitic magmatism in the Kola Alkaline Province: A review. 1522
 1523 *Lithos* 85, 48–75. doi:10.1016/j.lithos.2005.03.020.
 1524 Droop, G.T.R., 1987. A general equation for estimating Fe³⁺ concen- 1524
 1525 trations in ferromagnesian silicates and oxides from microprobe 1525
 1526 analyses, using stoichiometric criteria. *Mineralogical magazine* 51, 431–435.
 1527 Dygert, N., Liang, Y., Sun, C., Hess, P., 2014. An experimen- 1527
 1528 tal study of trace element partitioning between augite and Fe- 1528
 1529 rich basalts. *Geochimica et Cosmochimica Acta* 132, 170–186. 1529
 1530 doi:10.1016/j.gca.2014.01.042.
 1531 Edgar, C.J., Wolff, J.A., Olin, P.H., Nichols, H.J., Pittari, A., Cas, 1530
 1531 R.A.F., Reiners, P.W., Spell, T.L., Martí, J., 2007. The late Qua- 1531
 1532 ternary Diego Hernandez Formation, Tenerife: Volcanology of 1532
 1533 a complex cycle of voluminous explosive phonolitic eruptions. 1532
 1534

- Journal of Volcanology and Geothermal Research 160, 59–85. doi:10.1016/j.jvolgeores.2006.06.001.
- Eugster, H.P., Wones, D.R., 1962. Stability relations of the ferruginous biotite, annite. Journal of Petrology 3, 82–125. doi:10.1093/petrology/3.1.82.
- Fedele, L., Zanetti, A., Morra, V., Lustrino, M., Melluso, L., Vanucci, R., 2009. Clinopyroxene/liquid trace element partitioning in natural trachyte–trachyphonolite systems: insights from Campi Flegrei (southern Italy). Contributions to Mineralogy and Petrology 158, 337–356. doi:10.1007/s00410-009-0386-5.
- Foley, S.F., Prelevic, D., Rehfeldt, T., Jacob, D.E., 2013. Minor and trace elements in olivines as probes into early igneous and mantle melting processes. Earth and Planetary Science Letters 363, 181–191. doi:10.1016/j.epsl.2012.11.025.
- Francis, D., Minarik, W., 2008. Aluminum-dependent trace element partitioning in clinopyroxene. Contributions to Mineralogy and Petrology 156, 439–451. doi:10.1007/s00410-008-0295-z.
- Gaetani, G.A., 2004. The influence of melt structure on trace element partitioning near the peridotite solidus. Contributions to Mineralogy and Petrology 147, 511–527. doi:10.1007/s00410-004-0575-1.
- Gaetani, G.A., Grove, T.L., 1995. Partitioning of rare earth elements between clinopyroxene and silicate melt: Crystal-chemical controls. Geochimica et Cosmochimica Acta 59, 1951–1962. doi:10.1016/0016-7037(95)00119-0.
- Gaillard, F., Scaillet, B., Pichavant, M., 2002. Kinetics of iron oxidation-reduction in hydrous silicic melts. American Mineralogist 87, 829–837. doi:10.2138/am-2002-0704.
- Giehl, C., Marks, M., Nowak, M., 2013. Phase relations and liquid lines of descent of an iron-rich peralkaline phonolitic melt: an experimental study. Contributions to Mineralogy and Petrology 165, 283–304. doi:10.1007/s00410-012-0809-6.
- Giordano, D., Nichols, A., Dingwell, D., 2005. Glass transition temperatures of natural hydrous melts: a relationship with shear viscosity and implications for the welding process. Journal of Volcanology and Geothermal Research 142, 105–118. doi:10.1016/j.jvolgeores.2004.10.015.
- Girnis, A.V., Bulatov, V.K., Brey, G.P., Gerdes, A., Höfer, H.E., 2013. Trace element partitioning between mantle minerals and silico-carbonate melts at 6–12 GPa and applications to mantle metasomatism and kimberlite genesis. Lithos 160–161, 183–200. doi:10.1016/j.lithos.2012.11.027.
- Goodenough, K.M., Schilling, J., Jonsson, E., Kalvig, P., Charles, N., Tuduri, J., Deady, E.A., Sadeghi, M., Schiellerup, H., Müller, A., Bertrand, G., Arvanitidis, N., Eliopoulos, D.G., Shaw, R.A., Thrane, K., Keulen, N., 2016. Europe's rare earth element resource potential: An overview of REE metallogenetic provinces and their geodynamic setting. Ore Geology Reviews 72, 838–856. doi:10.1016/j.oregeorev.2015.09.019.
- Grove, T.L., Baker, M.B., Kinzler, R.J., 1984. Coupled CaAl-NaSi diffusion in plagioclase feldspar: Experiments and applications to cooling rate speedometry. Geochimica et Cosmochimica Acta 48, 2113–2121. doi:10.1016/0016-7037(84)90391-0.
- Guillou, H., Carracedo, J.C., Paris, R., Pérez Torrado, F.J., 2004. Implications for the early shield-stage evolution of Tenerife from K/Ar ages and magnetic stratigraphy. Earth and Planetary Science Letters 222, 599–614. doi:10.1016/j.epsl.2004.03.012.
- Gureenko, A.A., Hoernle, K.A., Hauff, F., Schmincke, H.U., Han, D., Miura, Y.N., Kaneoka, I., 2006. Major, trace element and NdSrPbOHeAr isotope signatures of shield stage lavas from the central and western Canary Islands: Insights into mantle and crustal processes. Chemical Geology 233, 75–112. doi:10.1016/j.chemgeo.2006.02.016.
- Hanchar, J.M., Finch, R.J., Hoskin, P.W.O., Watson, E.B., Cherniak, D.J., Mariano, A.N., 2001. Rare earth elements in synthetic zircon: Part 1. Synthesis, and rare earth element and phosphorus doping. American Mineralogist 86, 667–680. doi:10.1130/0091-7613(1990)018;0757:CTOGAS;2.3.CO;2.
- Hazen, R.M., Finger, L.W., 1979. Bulk modulus-volume relationship for cation-anion polyhedra. Journal of Geophysical Research: Solid Earth 84, 6723–6728. doi:10.1029/JB084iB12p06723.
- Hill, E., Blundy, J.D., Wood, B.J., 2011. Clinopyroxene-melt trace element partitioning and the development of a predictive model for HFSE and Sc. Contributions to Mineralogy and Petrology 161, 423–438. doi:10.1007/s00410-010-0540-0.
- Hill, E., Wood, B.J., Blundy, J.D., 2000. The effect of Ca-Tschermaks component on trace element partitioning between clinopyroxene and silicate melt. Lithos 53, 203–215. doi:10.1016/S0024-4937(00)00025-6.
- Huang, F., Lundstrom, C.C., McDonough, W.F., 2006. Effect of melt structure on trace-element partitioning between clinopyroxene and silicic, alkaline, aluminous melts. American Mineralogist 91, 1385–1400. doi:10.2138/am.2006.1909.
- Jugo, P.J., Wilke, M., Botcharnikov, R.E., 2010. Sulfur K-edge XANES analysis of natural and synthetic basaltic glasses: Implications for S speciation and S content as function of oxygen fugacity. Geochimica et Cosmochimica Acta 74, 5926–5938. doi:10.1016/j.gca.2010.07.022.
- Kennedy, A.K., Lofgren, G.E., Wasserburg, G.J., 1993. An experimental study of trace element partitioning between olivine, orthopyroxene and melt in chondrules: equilibrium values and kinetic effects. Earth and Planetary Science Letters 115, 177–195. doi:10.1016/0012-821X(93)90221-T.
- Kogarko, L.N., 1990. Ore-forming potential of alkaline magmas. Lithos 26, 167–175. doi:10.1016/0024-4937(90)90046-4.
- Kovalenko, V.I., Hervig, R.L., Sheridan, M.F., 1988. Ion microprobe analyses of trace elements in anorthoclase, hedenbergite, aenigmatite, quartz, apatite and glass in pantellerite: evidence for high water contents in pantellerite melt. American Mineralogist 73, 1038–1045.
- Kress, V.C., Carmichael, I.S.E., 1991. The compressibility of silicate liquids containing Fe₂O₃ and the effect of composition, temperature, oxygen fugacity and pressure on their redox states. Contributions to Mineralogy and Petrology 108, 82–92. doi:10.1007/BF00307328.
- Kumazawa, M., 1969. The elastic constants of single-crystal orthopyroxene. Journal of Geophysical Research 74, 5973–5980. doi:10.1029/JB074i025p05973.
- Larsen, L.M., 1979. Distribution of REE and other trace elements between phenocrysts and peralkaline undersaturated magmas, exemplified by rocks from the Gardar igneous province, south Greenland. Lithos 12, 303–315. doi:10.1016/0024-4937(79)90022-7.
- Law, K.M., Blundy, J.D., Wood, B.J., Ragnarsdottir, K.V., 2000. Trace element partitioning between wollastonite and silicate-carbonate melt. Mineralogical Magazine 64, 651–661. doi:10.1180/002646100549670.
- Le Bas, M.J., Le Maitre, R.W., Streckeisen, A., Zanettin, B., 1986. A Chemical Classification of Volcanic Rocks Based on the Total Alkali-Silica Diagram. Journal of Petrology 27, 745–750. doi:10.1093/petrology/27.3.745.
- Liang, Y., Richter, F.M., Watson, E.B., 1994. Convection in multi-component silicate melts driven by coupled diffusion. Nature 369, 390–392. doi:10.1038/369390a0.
- Linnen, R.L., Keppler, H., 1997. Columbite solubility in granitic melts: consequences for the enrichment and fractionation of Nb and Ta in the Earth's crust. Contributions to Mineralogy and Petrology 128, 213–227. doi:10.1007/s004100050304.
- Lofgren, G., 1989. Dynamic crystallization of chondrule melts of porphyritic olivine composition: Textures experimental and natural. Geochimica et Cosmochimica Acta 53, 461–470.

- 1669 doi:10.1016/0016-7037(89)90397-9. 1734
- 1670 Lofgren, G.E., Huss, G.R., Wasserburg, G.J., 2006. An ex- 1735
1671 perimental study of trace-element partitioning between Ti-Al- 1736
1672 clinopyroxene and melt: Equilibrium and kinetic effects in- 1737
1673 cluding sector zoning. *American Mineralogist* 91, 1596–1606. 1738
1674 doi:10.2138/am.2006.2108. 1739
- 1675 Lu, F., Anderson, A.T., Davis, A.M., 1995. Diffusional gradients at 1740
1676 the crystal / melt interface and their effect on the compositions of 1741
1677 melt inclusions. *The Journal of Geology* 103, 591–597. 1742
- 1678 Lundstrom, C.C., Shaw, H.F., Ryerson, F.J., Phinney, D.L., Gill, 1743
1679 J.B., Williams, Q., 1994. Compositional controls on the parti- 1744
1680 tioning of U, Th, Ba, Pb, Sr and Zr between clinopyroxene and 1745
1681 haplobasaltic melts: implications for uranium series disequilib- 1746
1682 ria in basalts. *Earth and Planetary Science Letters* 128, 407–423. 1747
1683 doi:10.1016/0012-821X(94)90159-7. 1748
- 1684 Mahood, G.A., Stímac, J.A., 1990. Trace-element partitioning in pan- 1749
1685 tellerites and trachytes. *Geochimica et Cosmochimica Acta* 54, 1750
1686 2257–2276. doi:10.1016/0016-7037(90)90050-U. 1751
- 1687 Marks, M., Halama, R., Wenzel, T., Markl, G., 2004. Trace el- 1752
1688 ement variations in clinopyroxene and amphibole from alkaline 1753
1689 to peralkaline syenites and granites: implications for mineral- 1754
1690 melt trace-element partitioning. *Chemical Geology* 211, 185–215. 1755
1691 doi:10.1016/j.chemgeo.2004.06.032. 1756
- 1692 Marks, M., Markl, G., 2001. Fractionation and assimilation processes 1757
1693 in the alkaline augite syenite unit of the Ilímaussaq intrusion, south 1758
1694 Greenland, as deduced from phase equilibria. *Journal of Petrology* 1759
1695 42, 1947–1969. doi:10.1093/petrology/42.10.1947. 1760
- 1696 Marks, M., Markl, G., 2003. Ilímaussaq en miniature': closed- 1761
1697 system fractionation in an agpaitic dyke rock from the Gar- 1762
1698 dar Province, South Greenland (contribution to the mineralogy 1763
1699 of Ilímaussaq no. 117). *Mineralogical Magazine* 67, 893–919. 1764
1700 doi:10.1180/0026461036750150. 1765
- 1701 Marks, M.A., Markl, G., 2017. A global review on ag- 1766
1702 patic rocks. *Earth-Science Reviews* 173, 229–258. 1767
1703 doi:10.1016/j.earscirev.2017.06.002. 1768
- 1704 Marks, M.A.W., Hettmann, K., Schilling, J., Frost, B.R., Markl, 1769
1705 G., 2011. The mineralogical diversity of alkaline igneous 1770
1706 rocks: Critical factors for the transition from miaskitic to ag- 1771
1707 patic phase assemblages. *Journal of Petrology* 52, 439–455. 1772
1708 doi:10.1093/petrology/eqq086. 1773
- 1709 Möller, V., Williams-Jones, A.E., 2016. Petrogenesis of the Nechala- 1774
1710 cho Layered Suite, Canada: magmatic Evolution of a REE-Nb-rich 1775
1711 Nepheline Syenite Intrusion. *Journal of Petrology* 57, 229–276. 1776
1712 doi:10.1093/petrology/egw003. 1777
- 1713 Mollo, S., Blundy, J.D., Giacomoni, P., Nazzari, M., Scar- 1778
1714 lato, P., Coltorti, M., Langone, A., Andronico, D., 2017. 1779
1715 Clinopyroxene-melt element partitioning during interaction be- 1780
1716 tween trachybasaltic magma and siliceous crust: Clues from 1781
1717 quartzite enclaves at Mt. Etna volcano. *Lithos* 284–285, 447–461. 1782
1718 doi:10.1016/j.lithos.2017.05.003. 1783
- 1719 Mollo, S., Blundy, J.D., Iezzi, G., Scarlato, P., Langone, A., 1784
1720 2013. The partitioning of trace elements between clinopyrox- 1785
1721 ene and trachybasaltic melt during rapid cooling and crystal 1786
1722 growth. *Contributions to Mineralogy and Petrology* 166, 1633– 1787
1723 1654. doi:10.1007/s00410-013-0946-6. 1788
- 1724 Mollo, S., Forni, F., Bachmann, O., Blundy, J.D., De Astis, G., Scar- 1789
1725 lato, P., 2016. Trace element partitioning between clinopyrox- 1790
1726 ene and trachy-phonolitic melts: A case study from the Campan- 1791
1727 ian Ignimbrite (Campi Flegrei, Italy). *Lithos* 252253, 160–172. 1792
1728 doi:10.1016/j.lithos.2016.02.024. 1793
- 1729 Moore, G., Vennemann, T., Carmichael, I.S.E., 1998. An empirical 1794
1730 model for the solubility of H₂O in magmas to 3 kilobars. *American 1795
1731 Mineralogist* 83, 36–42. doi:10.1016/0012-821X(73)90129-5. 1796
- 1732 Morimoto, N., 1989. Nomenclature of pyroxenes. *Mineralogical Jour-* 1797
1733 *nal* 14, 198–221. doi:10.2465/minerj.14.198. 1798
- Mungall, J., Brenan, J., 2014. Partitioning of platinum-group 1734
elements and Au between sulfide liquid and basalt and the 1735
origins of mantle-crust fractionation of the chalcophile ele- 1736
ments. *Geochimica et Cosmochimica Acta* 125, 265–289. 1737
doi:10.1016/j.gca.2013.10.002.
- Mysen, B.O., Virgo, D., Seifert, F.A., 1982. The structure of 1738
silicate melts: Implications for chemical and physical proper- 1739
ties of natural magma. *Reviews of Geophysics* 20, 353–383. 1740
doi:10.1029/RG020i003p00353.
- Mysen, B.O., Virgo, D., Seifert, F.A., 1985. Relationships between 1741
properties and structure of aluminosilicate melts. *American Min- 1742
eralogist* 70, 88–105. doi:10.1007/BF00413348.
- Niu, Y., 2004. Bulk-rock major and trace element compositions of 1743
abyssal peridotites: Implications for mantle melting, melt extrac- 1744
tion and post-melting processes beneath Mid-Ocean ridges. *Jour- 1745
nal of Petrology* 45, 2423–2458. doi:10.1093/petrology/egh068.
- Olin, P.H., Wolff, J.A., 2010. Rare earth and high field strength ele- 1746
ment partitioning between iron-rich clinopyroxenes and felsic liq- 1747
uids. *Contributions to Mineralogy and Petrology* 160, 761–775. 1748
doi:10.1007/s00410-010-0506-2.
- Onuma, N., Higuchi, H., Wakita, H., Nagasawa, H., 1968. Trace el- 1749
ement partition between two pyroxenes and the host lava. *Earth 1750
and Planetary Science Letters* 5, 47–51. doi:10.1016/S0012- 1751
821X(68)80010-X.
- Paton, C., Hellstrom, J., Paul, B., Woodhead, J., Hergt, J., 2011. Iolite: 1752
1753 Freeware for the visualisation and processing of mass spectrometric 1754
data. *Journal of Analytical Atomic Spectrometry* 26, 2508– 1755
2518. doi:10.1039/C1JA10172B.
- Peters, S.T., Troll, V.R., Weis, F.A., Dallai, L., Chadwick, J.P., Schulz, 1756
B., 2017. Amphibole megacrysts as a probe into the deep plumbing 1757
system of Merapi volcano, Central Java, Indonesia. *Contributions 1758
to Mineralogy and Petrology* 172, 1–20. doi:10.1007/s00410-017- 1759
1338-0.
- Prowatke, S., Klemme, S., 2005. Effect of melt composition 1760
on the partitioning of trace elements between titanite and sil- 1761
icate melt. *Geochimica et Cosmochimica Acta* 69, 695–709. 1762
doi:10.1016/j.gca.2004.06.037.
- Putirka, K.D., 2008. Thermometers and Barometers for Volcanic 1763
Systems. *Reviews in Mineralogy and Geochemistry* 69, 61–120. 1764
doi:10.2138/rmg.2008.69.3.
- Rapp, R.P., Watson, E.B., 1986. Monazite solubility and dissolution 1765
kinetics: implications for the thorium and light rare earth chemistry 1766
of felsic magmas. *Contributions to Mineralogy and Petrology* 94, 1767
304–316. doi:10.1007/BF00371439.
- Rasband, W., 2016. ImageJ, U.S. National Institutes of Health, 1768
Bethesda, Maryland, USA.
- Redhammer, G.J., Amthauer, G., Roth, G., Tippelt, G., Lottermoser, 1769
W., 2006. Single-crystal X-ray diffraction and temperature depen- 1770
1771 dent 57Fe Mössbauer spectroscopy on the hedenbergite-aegirine 1772
(Ca,Na)(Fe₂₊,Fe₃₊)Si₂O₆ solid solution. *American Mineralogist* 1773
91, 1271–1292. doi:10.2138/am.2006.2173.
- Reguir, E.P., Chakhmouradian, A.R., Pisiak, L., Halden, N.M., Yang, 1774
P., Xu, C., Kynický, J., Couëslan, C.G., 2012. Trace-element com- 1775
position and zoning in clinopyroxene- and amphibole-group min- 1776
erals: Implications for element partitioning and evolution of car- 1777
bonatites. *Lithos* 128, 27–45. doi:10.1016/j.lithos.2011.10.003.
- Rubatto, D., Hermann, J., 2007. Experimental zircon/melt and 1778
1779 zircon/garnet trace element partitioning and implications for the 1780
geochronology of crustal rocks. *Chemical Geology* 241, 38–61. 1781
doi:10.1016/j.chemgeo.2007.01.027.
- Schmidt, B.C., Behrens, H., 2008. Water solubility in phonolite melts: 1782
Influence of melt composition and temperature. *Chemical Geology* 1783
256, 259–268. doi:10.1016/j.chemgeo.2008.06.043.
- Schmidt, K.H., Bottazzi, P., Vannucci, R., Mengel, K., 1999. Trace el- 1784
ement partitioning between phlogopite, clinopyroxene and leucite 1785

- 1799 lamproite melt. *Earth and Planetary Science Letters* 168, 287–299. doi:10.1016/S0012-821X(99)00056-4.
- 1800 Schmidt, M.W., Connolly, J.A.D., Günther, D., Bogaerts, M., 2006. Element partitioning: The role of melt structure and composition. *Science* 312, 1646–1650. doi:10.1126/science.1126690.
- 1801 Severs, M.J., Beard, J.S., Fedele, L., Hanchar, J.M., Mutchler, S.R., Bodnar, R.J., 2009. Partitioning behavior of trace elements between dacitic melt and plagioclase, orthopyroxene, and clinopyroxene based on laser ablation ICPMS analysis of silicate melt inclusions. *Geochimica et Cosmochimica Acta* 73, 2123–2141. doi:10.1016/j.gca.2009.01.009.
- 1802 Shannon, R., 1976. Revised effective ionic radii and systematic studies of interatomic distances in halides and chalcogenides. *Acta Crystallographica Section A* 32, 751–767.
- 1803 Shea, T., Hammer, J.E., 2013. Kinetics of cooling- and decompression-induced crystallization in hydrous mafic-intermediate magmas. *Journal of Volcanology and Geothermal Research* 260, 127–145. doi:10.1016/j.jvolgeores.2013.04.018.
- 1804 Shearer, C.K., Larsen, L.M., 1994. Sector-zoned aegirine from the Ilmaussaq alkaline intrusion, South Greenland; implications for trace-element behavior in pyroxene. *American Mineralogist* 79, 340–352.
- 1805 Sjöqvist, A., Cornell, D., Andersen, T., Erambert, M., Ek, M., Leijd, M., 2013. Three compositional varieties of rare-earth element ore: Eudialyte-group minerals from the Norra Kärr alkaline complex, Southern Sweden. *Minerals* 3, 94–120. doi:10.3390/min3010094.
- 1806 Sørensen, H., 1992. Agpaitic nepheline syenites: a potential source of rare elements. *Applied Geochemistry* 7, 417–427. doi:10.1016/0883-2927(92)90003-L.
- 1807 Spera, F.J., Bohrson, W.A., 2001. Energy-constrained open-system magmatic processes I: General model and energy-constrained assimilation and fractional crystallization (EC-AFC) formulation. *Journal of Petrology* 42, 999–1018. doi:10.1093/petrology/42.5.999.
- 1808 Stevens, J., 1996. Applied multivariate analysis for the social sciences. Lawrence Erlbaum, Mahwah, NJ.
- 1809 Sun, C., Liang, Y., 2012. Distribution of REE between clinopyroxene and basaltic melt along a mantle adiabat: Effects of major element composition, water, and temperature. *Contributions to Mineralogy and Petrology* 163, 807–823. doi:10.1007/s00410-011-0700-x.
- 1810 Thirlwall, M.F., Singer, B.S., Marriner, G.F., 2000. ^{39}Ar – ^{40}Ar ages and geochemistry of the basaltic shield stage of Tenerife, Canary Islands, Spain. *Journal of Volcanology and Geothermal Research* 103, 247–297. doi:10.1016/S0377-0273(00)00227-4.
- 1811 Troll, V., Schmincke, H., 2002. Magma mixing and crustal recycling recorded in ternary feldspar from compositionally zoned peralkaline ignimbrite 'A', Gran Canaria, Canary Islands. *Journal of Petrology* 43, 243–270. doi:10.1093/petrology/43.2.243.
- 1812 Van Orman, J.A., Grove, T.L., Shimizu, N., 2001. Rare earth element diffusion in diopside: influence of temperature, pressure, and ionic radius, and an elastic model for diffusion in silicates. *Contributions to Mineralogy and Petrology* 141, 687–703. doi:10.1007/s004100100269.
- 1813 Walker, D., Kirkpatrick, R.J., Longhi, J., Hays, J.F., 1976. Crystallization history of lunar picritic basalt sample 12002: Phase-equilibria and cooling-rate studies. *Bulletin of the Geological Society of America* 87, 646–656. doi:10.1130/0016-7606.
- 1814 Watson, E.B., 1979. Zircon saturation in felsic liquids: Experimental results and applications to trace element geochemistry. *Contributions to Mineralogy and Petrology* 70, 407–419. doi:10.1007/BF00371047.
- 1815 Weidner, D.J., Vaughan, M.T., 1982. Elasticity of pyroxenes: Effects of composition versus crystal structure. *Journal of Geophysical Research* 87, 9349–9353.
- 1816 Wiesmaier, S., Troll, V.R., Carracedo, J.C., Ellam, R.M., Bindeman, I., Wolff, J.A., 2012. Bimodality of lavas in the Teide–Pico Viejo Succession in Tenerife—the role of crustal melting in the origin of recent phonolites. *Journal of Petrology* 53, 2465–2495. doi:10.1093/petrology/egs056.
- 1817 Wood, B.J., Blundy, J.D., 1997. A predictive model for rare earth element partitioning between clinopyroxene and anhydrous silicate melt. *Contributions to Mineralogy and Petrology* 129, 166–181. doi:10.1007/s004100050330.
- 1818 Wood, B.J., Blundy, J.D., 2001. The effect of cation charge on crystal-melt partitioning of trace elements. *Earth and Planetary Science Letters* 188, 59–71. doi:10.1016/S0012-821X(01)00294-1.
- 1819 Wood, B.J., Blundy, J.D., 2003. Trace element partitioning under crustal and uppermost mantle conditions: The influences of ionic radius, cation charge, pressure, and temperature, in: Carlson, R.W. (Ed.), *The Mantle and Core: Treatise on Geochemistry*. Elsevier. volume 2, chapter 2.09, pp. 395–424. doi:10.1016/B0-08-043751-6/02009-0.
- 1820 Wood, B.J., Blundy, J.D., 2014. Trace element partitioning: The influences of ionic radius, cation charge, pressure, and temperature, in: Carlson, R.W. (Ed.), *The Mantle and Core: Treatise on Geochemistry: Second Edition*. Elsevier. chapter 3.11, pp. 421–445. doi:10.1016/B978-0-08-095975-7.00206-0.
- 1821 Wood, B.J., Trigila, R., 2001. Experimental determination of alumino-clinopyroxene–melt partition coefficients for potassic liquids, with application to the evolution of the Roman province potassic magmas. *Chemical Geology* 172, 213–223. doi:10.1016/S0009-2541(00)00259-X.
- 1822 Workman, R.K., Hart, S.R., 2005. Major and trace element composition of the depleted MORB mantle (DMM). *Earth and Planetary Science Letters* 231, 53–72. doi:10.1016/j.epsl.2004.12.005.
- 1823 Wörner, G., Beusen, J.M., Duchateau, N., Gijbels, R., Schmincke, H.U., 1983. Trace element abundances and mineral/melt distribution coefficients in phonolites from the Laacher See volcano (Germany). *Contributions to Mineralogy and Petrology* 84, 152–173. doi:10.1007/BF00371282.
- 1824 Xu, C., Kynicky, J., Chakhmouradian, A.R., Campbell, I.H., Allen, C.M., 2010. Trace-element modeling of the magmatic evolution of rare-earth-rich carbonatite from the Miaoya deposit, Central China. *Lithos* 118, 145–155. doi:10.1016/j.lithos.2010.04.003.
- 1825 Yang, L., van Hinsberg, V.J., Samson, I.M., 2018. A new method to deconvolute binary mixture in LA-ICP-MS analyses to quantify the composition of phases smaller than the laser spot size. *JAAS*.
- 1826 Yao, L., Sun, C., Liang, Y., 2012. A parameterized model for REE distribution between low-Ca pyroxene and basaltic melts with applications to REE partitioning in low-Ca pyroxene along a mantle adiabat and during pyroxenite-derived melt and peridotite interaction. *Contributions to Mineralogy and Petrology* 164, 261–280. doi:10.1007/s00410-012-0737-5.
- 1827 Zhang, Y., Ni, H., Chen, Y., 2010. Diffusion data in silicate melts. *Reviews in Mineralogy and Geochemistry* 72, 311–408. doi:10.2138/rmg.2010.72.8.

1915 **6. Tables**

Table 1: Major-element composition (in wt%) of starting materials for the internally heated pressure vessel experiments. The totals are calculated with all iron as FeO.

Dry starting glass compositions calculated from masses of reagents added [wt%]										
Composition	SiO ₂	TiO ₂	Al ₂ O ₃	FeOT	MgO	CaO	Na ₂ O	K ₂ O	Total	(Na+K)/Al
L4	57.48	1.50	19.00	5.89	1.61	3.21	7.33	3.98	100.00	0.861
L5	61.24	0.68	19.51	3.77	0.43	0.91	8.63	4.84	100.00	0.996
M3	52.67	2.27	18.13	7.86	2.75	5.40	7.19	3.73	100.00	0.875
M4	56.35	1.47	18.63	5.77	1.58	3.15	8.48	4.57	100.00	1.014
M5	60.04	0.66	19.13	3.69	0.42	0.89	9.76	5.41	100.00	1.145
H4	54.80	1.43	18.12	5.62	1.54	3.06	10.07	5.38	100.00	1.236
H5	58.38	0.65	18.60	3.59	0.41	0.86	11.31	6.20	100.00	1.362

Water saturated glass compositions from superliquidus experiments (EPMA) [wt%]										
L5	57.46	0.643	16.59	2.363	0.404	0.985	7.840	4.462	90.75	1.069
s.d. (n = 8)	0.299	0.087	0.210	0.059	0.035	0.050	0.175	0.132	0.351	0.017
rsd	0.52%	13.58%	1.26%	2.51%	8.70%	5.09%	2.23%	2.97%	0.39%	1.57%
H5	55.58	0.612	16.21	2.568	0.422	0.906	10.77	5.732	92.80	1.476
s.d. (n = 13)	0.327	0.057	0.221	0.113	0.044	0.049	0.205	0.154	0.417	0.028
rsd	0.59%	9.33%	1.36%	4.41%	10.44%	5.40%	1.90%	2.69%	0.45%	1.87%

Table 2: Summary of run conditions and run products for the internally-heated pressure vessel experiments.

Experiment	Setup	Pressure [bar]	Cooling ramp			Time		Run products
			Rate °C /min	Cycle +10°C	TE-1/TE-3 [°C]	TE-2 (spl)	[°C]	
L4 ₃	IHPV RQ (f)	2038	1	Y	825	828	44h50m	Cpx + Ox + Ttn + Melt
L5 ₃	IHPV RQ (f)	2038	1	Y	825	828	44h50m	Cpx + Ox + Melt
M3 ₂	IHPV RQ	2020	1	Y	796/795	799	47h	Cpx + Ox + Bt + Melt
M4 ₄	IHPV RQ	2020	1	Y	796/795	799	47h	Cpx + Ox + Bt + Melt
M5	IHPV	2000	-	-	800	799	47h55m	Cpx + Bt + Fsp + Melt
M5 ₂	IHPV RQ	2000	-	-	700	689	45h45m	Cpx + Bt + Fsp + Melt
H4 ₂	IHPV	2000	-	-	800	799	47h55m	Cpx + Ttn + Melt
H5 ₂	IHPV RQ	2000	-	-	700	689	45h45m	Cpx + Bt + Fsp + Melt
H5 ₃	IHPV RQ	2020	-	-	651/649	648	46h15m	Cpx + Bt + Fsp + Melt
NLS-9	IHPV RQ	2020	1	Y	651/649	648	46h15m	Cpx + Ox + Melt
NLS-9 ₂ HM	IHPV RQ**	2000	1	Y	650	655	42h	Cpx + Ox + Fsp + Melt

(f) indicates failure of the rapid quench apparatus; ** indicates use of a haematite double capsule, for run conditions at the haematite-magnetite fO₂ buffer (Eugster and Wones, 1962). Cpx = clinopyroxene; Ox = spinel oxide; Ttn = titanite; Bt = biotite; Fsp = sanidine feldspar.

Table 3: Representative major-element compositions of clinopyroxene and melt for the performed internally heated pressure vessel experiments and Canary Islands phenocryst–glass pairs.

<i>Pyroxene</i>	L4 ₃	M3 ₂	M5 ₂	H5 ₃	NLS-9	NLS-9 ₂ <i>HM</i>	16-07 LMB	17-12 M. Samara	17-14 UMB-II	21-30 PV 2 ka
SiO ₂	44.70	40.73	47.31	46.95	50.73	51.90	52.43	51.77	51.81	52.50
TiO ₂	3.07	4.57	3.17	4.47	0.10	0.10	0.80	0.78	0.74	0.75
Al ₂ O ₃	5.23	9.26	3.08	3.10	2.46	2.96	1.33	1.24	1.27	1.22
FeO	13.31	11.72	18.84	16.95	28.14	28.61	9.71	9.62	10.51	10.02
MnO	0.01	0.01	0.01	0.00	0.25	0.17	0.78	0.84	0.91	0.81
MgO	9.09	9.28	5.55	6.05	0.05	0.07	12.30	12.64	12.07	11.88
CaO	19.49	22.17	16.11	15.29	5.88	3.14	21.90	21.76	21.52	22.02
Na ₂ O	2.27	1.01	4.34	4.97	9.86	11.45	1.18	1.17	1.38	1.19
K ₂ O	0.09	0.03	0.08	0.07	0.04	0.04	0.02	0.03	0.00	0.02
Total	97.25	98.78	98.49	97.85	97.49	98.45	100.44	99.85	100.22	100.42
<i>Glass</i>										
SiO ₂	58.79	57.29	57.45	54.91	58.17	58.14	60.38	55.10	59.08	60.04
TiO ₂	0.35	0.27	0.23	0.62	0.00	0.00	0.64	1.73	0.66	0.66
Al ₂ O ₃	17.35	19.14	16.69	16.06	18.55	19.41	19.96	18.30	19.68	19.79
Fe ₂ O ₃ (T)	2.35	1.35	1.01	3.16	1.67	1.91	3.65	7.22	4.02	3.96
FeO(T)	2.12	1.22	0.91	2.84	1.50	1.72	3.28	6.49	3.62	3.56
MnO	0.02	0.00	-	0.01	0.06	0.04	0.14	0.23	0.22	0.20
MgO	0.20	0.13	0.15	0.35	0.00	0.00	0.39	1.84	0.32	0.35
CaO	0.55	0.95	0.24	0.84	0.23	0.23	0.76	4.10	0.77	0.74
Na ₂ O	7.17	7.32	9.08	8.88	11.12	9.80	9.00	7.26	9.76	9.05
K ₂ O	4.68	4.10	4.68	5.30	1.51	2.51	5.41	4.09	5.45	5.57
Total	91.23	90.41	89.43	89.81	91.15	91.85	99.95	99.13	99.56	99.95
(Na+K)/Al	0.97	0.86	1.15	1.27	1.07	0.97	1.01	1.12	1.09	1.09

Table 4: Pyroxene–melt trace-element-partition coefficients for representative experiments and a natural phenocryst–glass pair.

-	L4 ₃ D	M3 ₂ D	M5 ₂ D	H5 ₃ D	NLS-9 D	NLS-9 ₂ <i>HM</i> D	16-07-px4 LMB D	
	σ	σ	σ	σ	σ	σ	σ	
Li	0.250	0.016	0.126	0.009	0.419	0.034	0.427	0.024
Ga	0.364	0.022	0.567	0.020	0.190	0.022	-	-
Rb	0.005	0.002	0.018	0.003	0.010	0.006	0.013	0.002
Sr	0.828	0.045	0.282	0.024	1.433	0.111	0.997	0.091
Y	5.577	0.302	13.784	1.949	1.814	0.236	1.102	0.060
Zr	1.699	0.082	2.537	0.222	1.361	0.089	1.164	0.083
Nb	0.126	0.085	0.889	0.258	0.554	0.280	1.688	0.196
Cs	0.019	0.003	0.019	0.003	0.014	0.006	0.010	0.002
Ba	0.0364	0.0087	0.0373	0.0152	0.0388	0.0261	0.0288	0.0091
La	4.787	0.646	2.591	0.240	4.658	0.962	3.049	0.132
Ce	7.199	0.756	6.229	0.646	5.199	1.073	3.190	0.129
Nd	16.105	1.537	28.430	4.210	6.454	1.630	3.759	0.147
Sm	17.843	1.414	47.245	7.699	5.215	1.293	3.113	0.137
Eu	16.403	1.341	53.195	8.181	4.743	1.132	2.900	0.133
Dy	9.027	0.537	27.082	3.925	2.619	0.460	1.521	0.073
Tm	4.773	0.261	9.067	0.903	2.937	0.279	1.567	0.097
Yb	4.797	0.249	7.015	0.600	3.937	0.296	2.281	0.152
Hf	2.385	0.162	3.556	0.472	1.802	0.118	1.141	0.123
Ta	0.496	0.152	2.3694	0.6244	0.6502	0.2545	1.5654	0.2337
Pb	0.079	0.017	0.0587	0.0152	0.1142	0.0349	0.0199	0.0130
Th	0.201	0.034	0.3565	0.0419	0.3172	0.0321	0.2892	0.0239
U	-	-	0.0512	0.0331	0.1261	0.0272	0.0196	0.0103

Table 5: Coefficients for prediction of lattice-strain parameters for clinopyroxene M1 and M2 sites from clinopyroxene composition, temperature and pressure. Fitted vs. predicted lattice-strain parameters and partition coefficients are in Figures 12–13 and full multiple linear regression reports are available as supplementary data file S4.

Model for $\text{Ln}D_0$ M2 site (n = 82)			Model for $\text{Ln}D_0$, M1 site (n = 16)		
Parameter	Coefficient	σ	Parameter	Coefficient	σ
Intercept	4.52	0.91	Intercept	5	1
M1Ti	6.8	3	TAl	4	0.5
M1Al - M1Fe ³⁺	1.6	0.6	M1Fe ²⁺	2.6	0.9
M2Fe ²⁺	-3.8	1.3	M2Na	-8	1
T [K]	-0.0035	0.0007	M2Ca	-3	2
TAl + TFe ³⁺	2.6	0.8			
R^2		0.647			0.959

Model for E_s , M2 site (n = 79)			Model for E_s , M1 site (n = 18)		
Parameter	Coefficient	σ	Parameter	Coefficient	σ
Intercept	247	44	Intercept	-2322	298
M1Al	-424	144	T [K]	3.2	0.4
M1Mg	-285	102	P [GPa]	-408	145
M1Ti	-1145	378	M1Mg	-800	212
M2Mg	-306	115			
P [GPa]	37	12			
TAl + TFe ³⁺	313	102			
XMg	336	102			
R^2		0.348			0.936

Model for r_0 , M2 site (n = 82)			Model for r_0 , M1 site (n = 16)		
Parameter	Coefficient	σ	Parameter	Coefficient	σ
Intercept	1.01	0.02	Intercept	0.79	0.03
M1Ti	0.16	0.05	P [GPa]	-0.017	0.005
M1Al-M1Fe ³⁺	-0.03	0.01	M2Mg	-0.48	0.06
M2Ca	0.09	0.02	M1Fe ³⁺	0.14	0.03
M2Na	0.14	0.02	M2Ca	-0.05	0.02
T [K]	-4.46E-05	1.22E-05			
R^2		0.846			0.987

1916 7. Supplementary figures

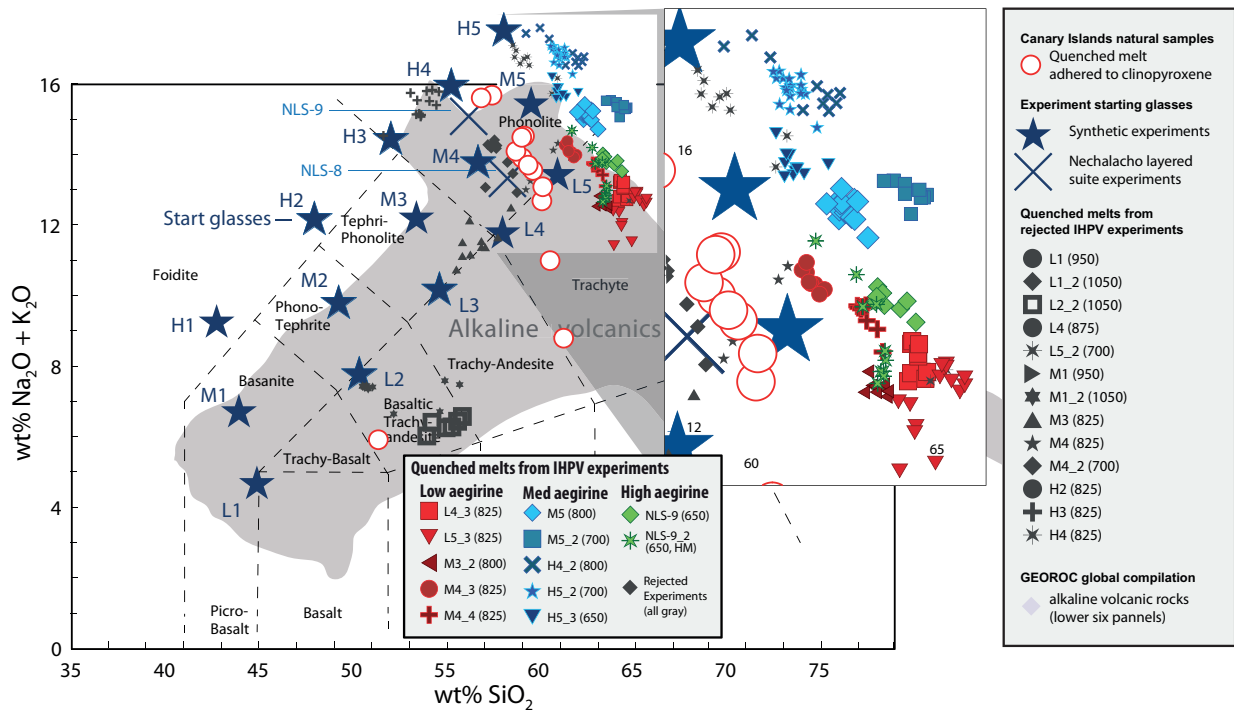


Figure S1: Total alkalies vs. silica diagram for glasses produced in internally heated pressure vessel experiments and adhered to Canary Islands clinopyroxene phenocrysts (Le Bas et al., 1986). Large stars indicate synthetic starting glass compositions as used in internally heated pressure vessel experiments (Table 1), whereas large crosses indicate the composition of powdered natural samples from the Nechalacho layered suite, NT, Canada that were used as starting materials for some experiments. The gray field indicates the compositional range expressed by alkaline volcanic provinces from around the world, sourced from the GEOROC database. Rejected experiments in dark gray are not discussed in the main text, and either did not produce clinopyroxene, produced crystals that were too small for analysis by LA-ICP-MS, or grew crystals during quench, hence preserving disequilibrium partitioning behaviour. Further diagrams showing major-element compositions for the quenched melts and the starting glasses are in Fig S2.

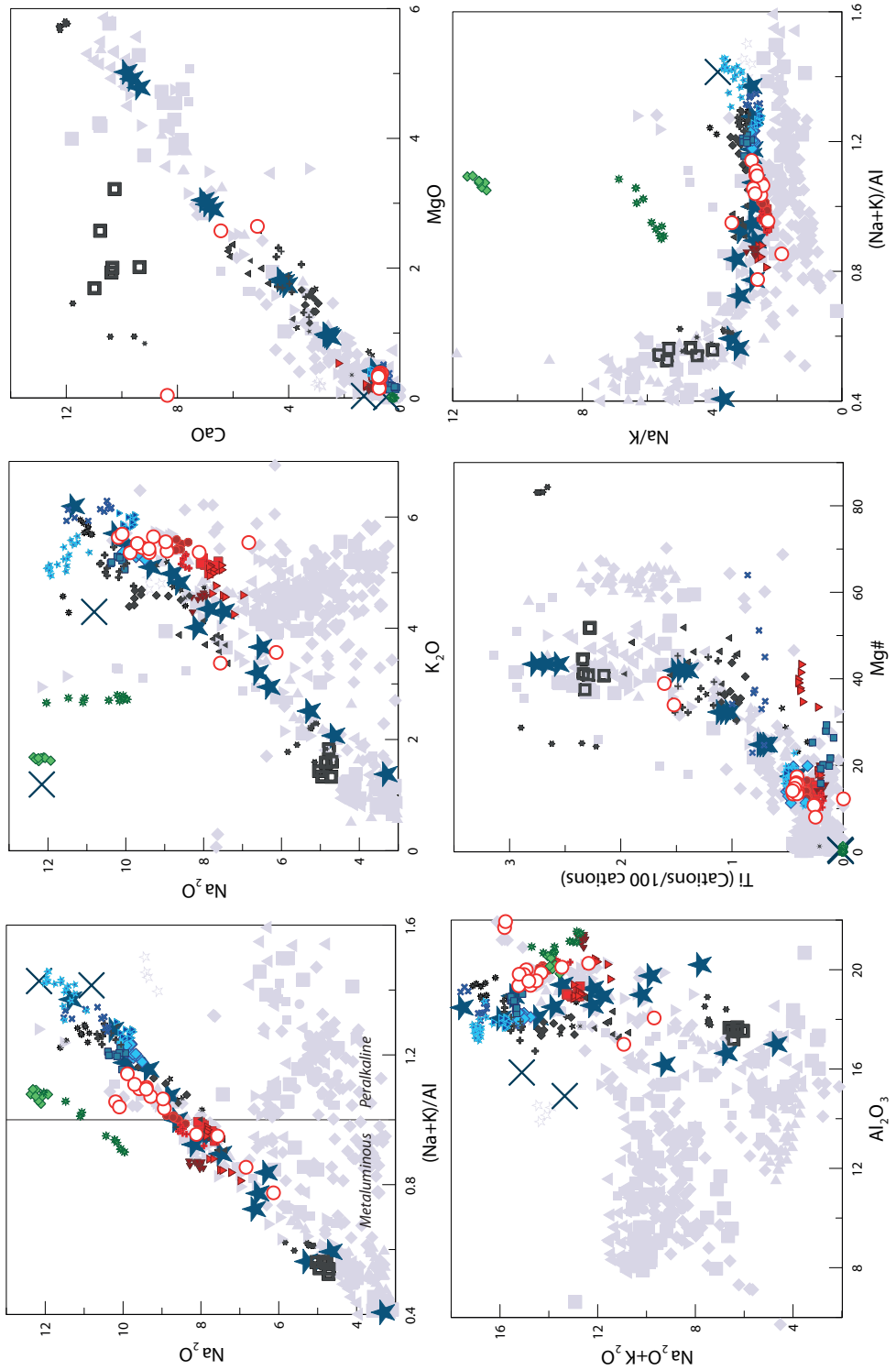


Figure S2: Major-element compositions for glass produced in the internally heated pressure vessel experiments and adhered to clinopyroxene phenocrysts from the Canary Islands. Symbols as in Fig. S1.

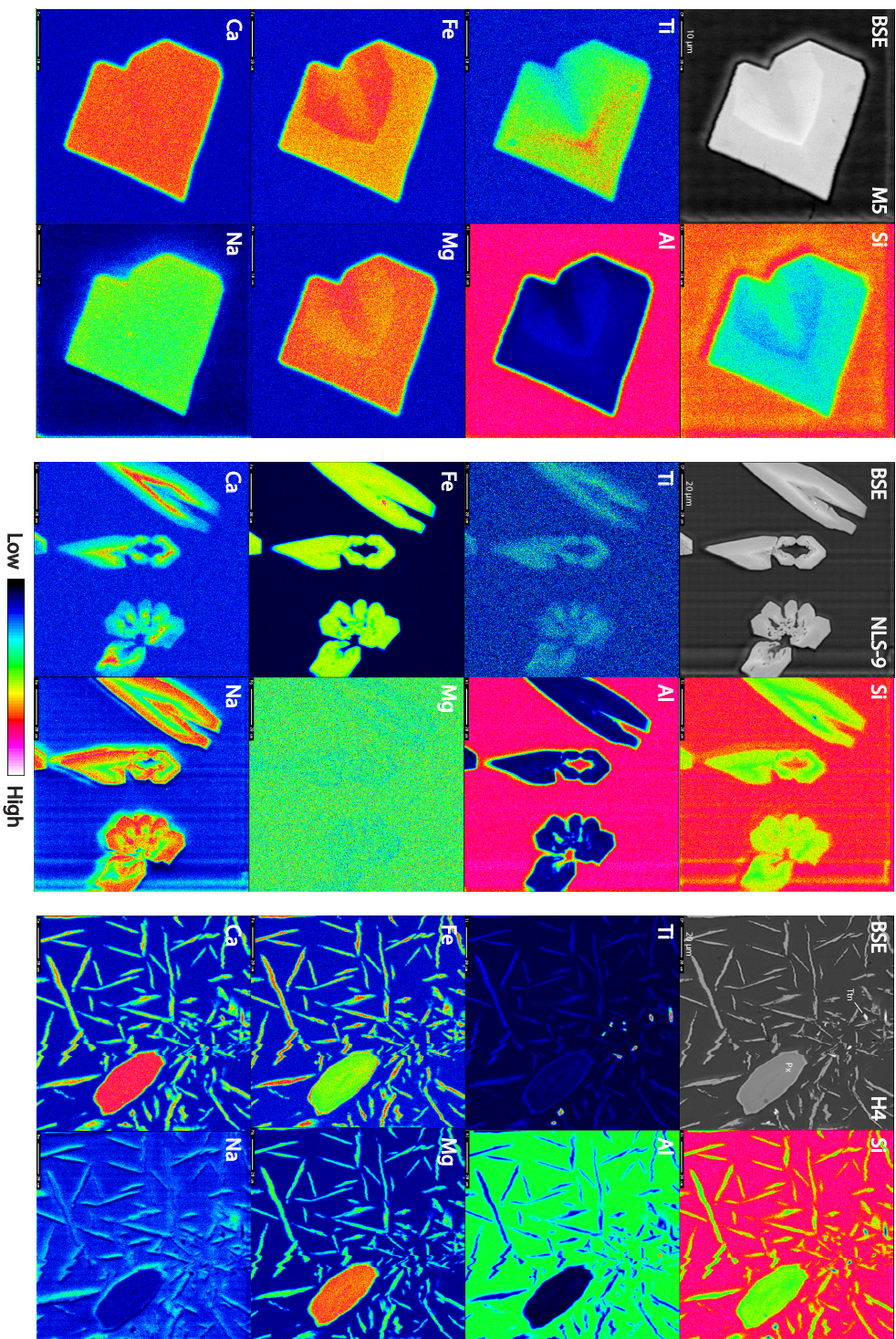


Figure S3: Element maps of clinopyroxene from internally heated pressure vessel experiments. M5 clinopyroxene have a sharp internal boundary that reflects feldspar saturation and are subtly zoned. NLS-9 clinopyroxene are more strongly zoned with swallowtail and hopper textures and rare inclusions of magnetite (cf. Walker et al., 1976; Lofgren, 1989; Shea and Hamner, 2013). H4 clinopyroxene (Px) display a bimodal crystal size distribution and occur with titanite (Tm). The bimodal crystal size distribution is due to a temperature perturbation during run, and renders this experiment unsuitable for this element-partitioning study.

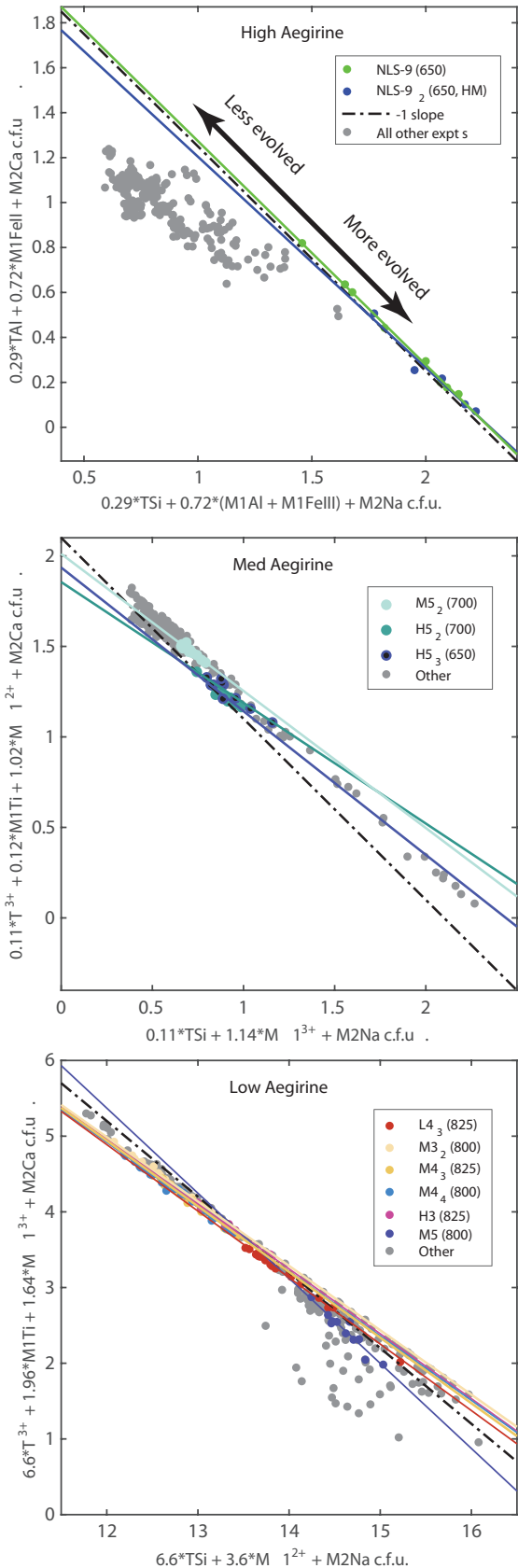


Figure S4: Major-element exchange mechanisms for (a) high, (b) medium and (c) low-aegirine clinopyroxene generated in internally heated pressure vessel experiments. Each individual plotted point represents an electron-microprobe analysis. Iron in the clinopyroxene was assigned to 2+ or 3+ valence following Droop (1987), then major-element cations were assigned to sites following Morimoto (1989, see supplement S5). Axes were defined by linear regressions between site-assigned major-element abundances, which have been checked for consistency in total site-occupancy and for charge.

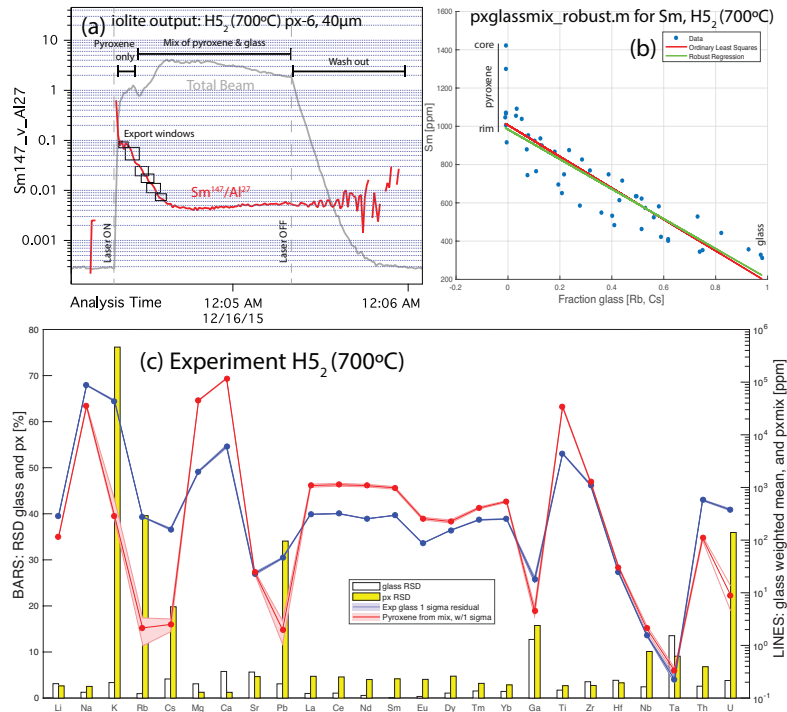


Figure S5: An example of the robust regression data reduction scheme for laser-ablation ICP-MS analyses of glass and clinopyroxene mixtures. (a) Time series of laser-ablation data, showing traces for Sm/Al (red) and total beam intensity (gray). The laser beam often ablated through the small clinopyroxene crystals, returning a mixed signal that was exported from the iolite data reduction software in short time windows as shown. Data were then normalised to the sum of major-element concentrations and mixes were deconvoluted using a robust regression script written in MATLAB. (b) An example output diagram for the robust regression data reduction scheme. Clinopyroxene–glass mixing ratios were constrained by strongly incompatible elements Rb and Cs. For each element, a robust linear regression was defined between the fraction of glass in the mixture and element concentration. The intercept of this regression with zero glass returned the trace-element concentrations in the clinopyroxene. Uncertainty with this technique is typically below 10 % relative (median 9.3 % at the 1 σ level). In this example, the Sm-rich core of a zoned clinopyroxene crystal is effectively rejected during data processing, and the derived Sm concentration for the clinopyroxene is therefore closer to that of the clinopyroxene rims that are in equilibrium with the adjacent quenched melt. (c) A quality control diagram output from the MATLAB data reduction scheme showing the concentrations of various elements in the glass and clinopyroxene (lines) and the uncertainty on these concentrations expressed as a relative standard deviation (bars). Derived partition coefficients (D_i) are the mass concentration of element ' i ' in clinopyroxene divided by that in the adjacent quenched melt. Residuals for the D_i values were calculated using uncertainties derived from the clinopyroxene and glass analyses to calculate minimum and maximum partition coefficients at the 1 σ level. These are reported in Table 4 and Supplement S1.

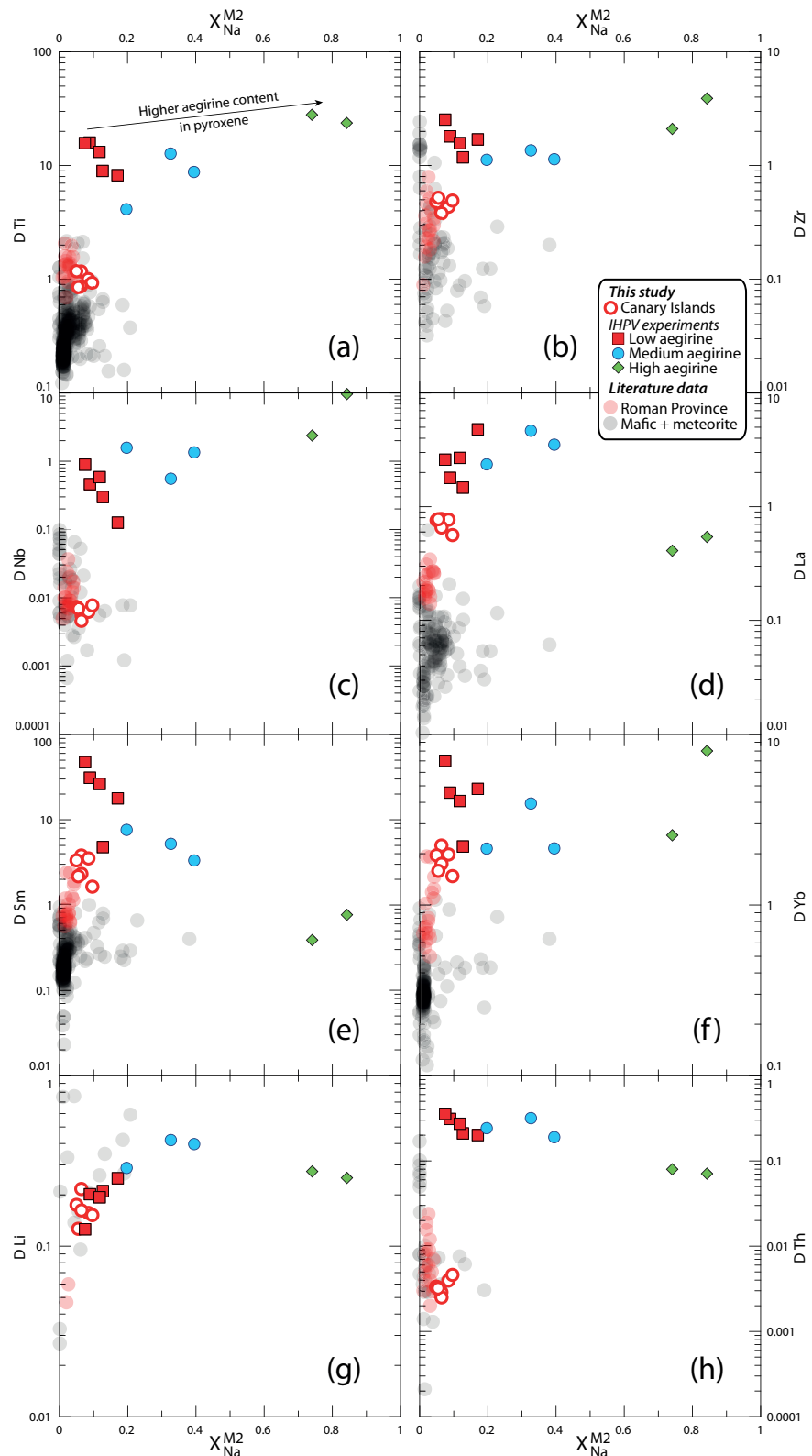


Figure S6: Element partitioning coefficients for HFSE (Ti, Zr, Nb), REE (La, Sm, Yb) and TE (Li, Th) vs. $X_{\text{Na}}^{\text{M2}}$. Literature values ($n = 411$), including those from the Roman Province, Italy, are from the compilation of Bédard (2014).

1917 **8. Electronic appendices**

xlsx

Table S1: Electronic appendix (.xlsx file) containing experiment starting glass compositions, experiment run conditions, mineral abundances in experimental charges, compositions of reference materials used for EPMA and LA-ICP analyses, major-element concentrations for experiment glasses and clinopyroxene, partition coefficients and fitted lattice-strain parameters.

kml

Table S2: Electronic appendix (.kml file) containing field locations for the Canary Islands samples.

kml

Table S3: Electronic appendix (.xlsx file) containing electron-microprobe transects across experiment clinopyroxene for Ce, Mg and Fe. The data indicate that $D_{Ce}^{px/melt}$ values determined from our experiments are overestimates, but only by up to 25%. Sector zoning in the clinopyroxene appears to have a larger impact on apparent Ce partitioning behaviour than growth zoning.

pdf

Table S4: Electronic appendix (.pdf file) containing multiple linear regression reports from the stepwise fitting of 3+ cation lattice-strain parameters for the predictive model for element-partitioning (39 pages).

xlsx

Table S5: Electronic appendix (.xlsx file) containing a numerical model for prediction of clinopyroxene/melt element-partitioning coefficients for ions of 3+ valence. Required input data are major-element oxide compositions for clinopyroxene, pressure and temperature. The model for the M2 site is calibrated for application to systems of basaltic to peralkaline phonolite composition. The model for the M1 site is calibrated for use on alkaline to weakly peralkaline systems where the aegirine mol% in clinopyroxene does not exceed 50.